

## The family of amide molecules toward NGC 6334I

NIELS F.W. LIGTERINK,<sup>1</sup> SAMER J. EL-ABD,<sup>2,3</sup> CRYSTAL L. BROGAN,<sup>3</sup> TODD R. HUNTER,<sup>3</sup> ANTHONY J. REMIJAN,<sup>3</sup>  
ROBIN T. GARROD,<sup>4</sup> AND BRETT M. MCGUIRE<sup>3,5</sup>

<sup>1</sup>*Center for Space and Habitability (CSH), University of Bern, Sidlerstrasse 5, 3012 Bern, Switzerland*

<sup>2</sup>*Department of Astronomy, University of Virginia, Charlottesville, VA 22904, USA*

<sup>3</sup>*National Radio Astronomy Observatory, Charlottesville, VA 22903, USA*

<sup>4</sup>*Departments of Chemistry and Astronomy, University of Virginia, Charlottesville, VA 22904, USA*

<sup>5</sup>*Harvard-Smithsonian Center for Astrophysics, Cambridge, MA 02138, USA*

### ABSTRACT

Amide molecules produced in space could play a key role in the formation of biomolecules on a young planetary object. However, the formation and chemical network of amide molecules in space is not well understood. In this work, ALMA observations are used to study a number of amide(-like) molecules toward the high-mass star-forming region NGC 6334I. The first detections of cyanamide (NH<sub>2</sub>CN), acetamide (CH<sub>3</sub>C(O)NH<sub>2</sub>) and N-methylformamide (CH<sub>3</sub>NHCHO) are presented for this source. These are combined with analyses of isocyanic acid (HNCO) and formamide (NH<sub>2</sub>CHO) and a tentative detection of urea (carbamide; NH<sub>2</sub>C(O)NH<sub>2</sub>). Abundance correlations show that most amides are likely formed in related reactions occurring in ices on interstellar dust grains in NGC 6334I. However, in an expanded sample of sources, large abundance variations are seen for NH<sub>2</sub>CN that seem to depend on the source type, which suggests that the physical conditions within the source heavily influence the production of this species. The rich amide inventory of NGC 6334I strengthens the case that interstellar molecules can contribute to the emergence of biomolecules on planets.

**Keywords:** Astrochemistry — Astrobiology — ISM: molecules — ISM: individual objects (NGC 6334I)

### 1. INTRODUCTION

Life as we know it relies on a select number of recurring chemical structures. Among these chemical structures, the amide unit (R<sub>1</sub>-C(=O)N-R<sub>2</sub>R<sub>3</sub>, see top panel of Fig. 1), is an essential component in numerous biomolecules. Notable examples are nucleobases, the molecules that encode RNA and DNA, and as the link in the peptide chains that form proteins. In order to understand the chemical origin of life, it is important to understand how molecules with an amide unit came to be on Earth. Chemical reactions on a young Earth can give rise to this class of molecules (e.g., Patel et al. 2015). However, a fascinating alternative is the formation of amides in space and subsequent delivery by, for example, meteorites to Earth (e.g., Chyba et al. 1990).

Several small amide molecules have been detected toward star and planet forming regions, most of them in

recent years, such as formamide (NH<sub>2</sub>CHO, Rubin et al. 1971), acetamide (CH<sub>3</sub>C(O)NH<sub>2</sub>, Hollis et al. 2006), and N-methylformamide (CH<sub>3</sub>NHCHO, Belloche et al. 2017, 2019). The first evidence for carbamide, also known as urea (NH<sub>2</sub>C(O)NH<sub>2</sub>), in the gas phase in the ISM comes from Remijan et al. (2014), but it was securely identified by Belloche et al. (2019). Molecules that are closely related to the amide structure have been observed as well. Examples are cyanamide<sup>1</sup> (NH<sub>2</sub>CN, Turner et al. 1975), isocyanic acid (HNCO, Snyder & Buhl 1972), and methyl isocyanate (CH<sub>3</sub>NCO, Halfen et al. 2015; Cernicharo et al. 2016; Ligterink et al. 2017). These molecules have structural similarities with biomolecules (see bottom panel of Fig. 1) and can act as precursor molecules to their formation.

<sup>1</sup> Throughout this work, for convenience cyanamide will be referred to as an amide, although strictly speaking it does not follow the chemical definition of an amide. See appendix A for an extended clarification on the naming and chemical structures of amides.

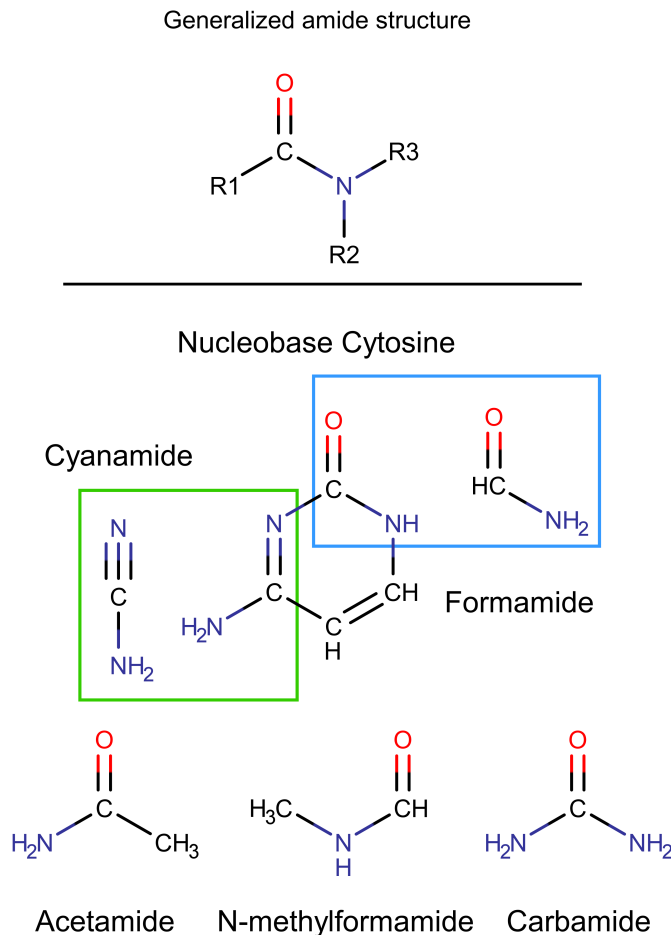


**Figure 1.** Top: Generalized structure of an amide. Various functional group can be attached to the  $\text{O}=\text{C}-\text{N}$  backbone on locations  $\text{R}_1$ ,  $\text{R}_2$ , and  $\text{R}_3$  ( $\text{R}$  represents any arbitrary atom or functional group, not a specific element). Bottom: Molecular structures of amides observed in space and that of the nucleobase cytosine. Structural similarities between cytosine and  $\text{NH}_2\text{CN}$  and  $\text{NH}_2\text{CHO}$  are highlighted.

To assess the importance of interstellar amides for biochemistry, it is important to know if they commonly occur in star- and planet-forming regions. The simplest amide  $\text{NH}_2\text{CHO}$  and related molecule  $\text{NH}_2\text{CN}$  have been detected toward a number of inter- and circumstellar sources (Belloche et al. 2020), including the sun-like protobinary IRAS 16293-2422 (Kahane et al. 2013; Coutens et al. 2016, 2018, hereafter IRAS 16293).  $\text{NH}_2\text{CHO}$  was also detected in comet 67P/Churyumov-Gerasimenko (Goesmann et al. 2015; Altwegg et al. 2017, hereafter 67P/C-G). However, larger amides have almost exclusively been observed toward the galactic center source Sagittarius B2 (hereafter Sgr B2, Halfen et al. 2011; Cernicharo et al. 2016; Ligterink et al. 2018a; Belloche et al. 2017, 2019).

An expanded sample of amide detections can help elucidate both their interstellar chemistry and the interplay of that chemistry with physical processes during star-formation. For example, a large sample of  $\text{HNCO}$  and  $\text{NH}_2\text{CHO}$  observations clearly shows an abundance correlation between these two species over a variety of sources (López-Sepulcre et al. 2019, and references therein). Hydrogenation (the addition of hydrogen atoms) of  $\text{HNCO}$  to form  $\text{NH}_2\text{CHO}$  has been proposed as a chemical explanation for the link between the two molecules (López-Sepulcre et al. 2015). However, recent modeling work indicates that the relation between the two molecules is rather due to similar responses of the formation pathways of each molecule to the physical environment (Quénard et al. 2018). Analogous analytical approaches could provide valuable insight into other amide species. But while chemical reactions for such molecules have recently been included in chemical networks (Belloche et al. 2017, 2019), observational constraints for these networks are sparse. To unravel interstellar amide chemistry and determine its relevance to biochemistry, it is important to expand the number of amide detections and to understand their formation. An ideal interstellar laboratory to study amides is found in the high-mass star-forming region (HMSFR) NGC 6334I. First, since the Solar System is thought to have formed in a massive cluster (e.g., Dukes & Krumholz 2012), NGC 6334I observations present a “direct” look at the conditions of early Solar System formation. Second, the chemistry of this region has been studied in great detail in the past decades, for example with the *Herschel Space Observatory* (Zernickel et al. 2012). In recent years, NGC 6334I has been extensively studied with the Atacama Large Millimeter Array (ALMA). This has not only resulted in a better understanding of the physical structure of this source (Brogan et al. 2016; Brogan et al. 2018), but also a better understanding of its molecular inventory. Various oxygen-bearing molecules have been investigated, including the  $\text{C}_2\text{H}_4\text{O}_2$  isomers methyl formate ( $\text{CH}_3\text{OCHO}$ ), glycolaldehyde ( $\text{HC}(\text{O})\text{CH}_2\text{OH}$ ), and acetic acid ( $\text{CH}_3\text{COOH}$ , McGuire et al. 2018; El-Abd et al. 2019; Xue et al. 2019), deuterated methanol (Bøgelund et al. 2018), and even the first ever interstellar detection of methoxymethanol ( $\text{CH}_3\text{OCH}_2\text{OH}$ , McGuire et al. 2017) in presented toward this source. Additionally, a number of complex nitrogen-bearing molecules were investigated by Bøgelund et al. (2019b), including  $\text{NH}_2\text{CHO}$ .

In this work, the inventory of amides toward NGC 6334I is investigated in detail. The first detections toward this object of  $\text{NH}_2\text{CN}$ ,  $\text{CH}_3\text{C}(\text{O})\text{NH}_2$ , and

$\text{CH}_3\text{NHCHO}$  are presented and combined with analysis of  $\text{HNCO}$  and  $\text{NH}_2\text{CHO}$ , and the tentative detection of  $\text{NH}_2\text{C(O)NH}_2$ . These observations and results are presented in section 2 and 3. The implications of the results are discussed in section 4, before giving the conclusions in section 5.

## 2. OBSERVATIONS AND ANALYSIS

### 2.1. *Observational Data of NGC 6334I*

In this work, ALMA observations of NGC 6334I in bands 4, 7, and 10 are analyzed. The details of the individual datasets and their reductions have been published in detail elsewhere (McGuire et al. 2017, 2018; Brogan et al. 2018) and will only be discussed briefly here. The pertinent observing parameters for each set of observations are provided in Table 2. The data were self-calibrated and continuum-subtracted following the procedures detailed in Hunter et al. (2017); Brogan et al. (2018). Prior to analysis, all of the observations were convolved to a common synthesized beam size of  $0.26'' \times 0.26''$ . From the data cubes, background temperatures ( $T_{\text{BG}}$ ) were determined based on the continuum level temperature and spectra were extracted for analysis at the same positions as used in El-Abd et al. (2019) and at an additional position called MM1-nmf. These positions are chosen to give an accurate overall sample of the chemistry toward NGC 6334I MM1 and MM2. The parameters of these positions are listed in Table 1 and are indicated on moment 0 maps shown in Fig. 2. In the case of Band 10 observations, robust analysis was only possible toward positions in MM1, as the MM2 source falls at the edge of the primary beam.

### 2.2. *Molecule identification & analysis*

All spectra are analyzed with the CASSIS<sup>2</sup> line analysis software. Line lists from the JPL catalog for molecular spectroscopy (Pickett et al. 1998), the Cologne Database for Molecular Spectroscopy (CDMS, Müller et al. 2001, 2005), and literature are used. For the molecules of interest to this work, that is amide and amide-like molecules, an overview of database and literature sources is given in Table 4 in Appendix B.

Given a line list and input parameters such as column density ( $N_s$ ), excitation temperature ( $T_{\text{ex}}$ ), source velocity ( $V_{\text{LSR}}$ ), and line width at full width at half maximum ( $\Delta V$ ), CASSIS is able to generate synthetic molecular spectra. Molecular line emission is coupled with the background temperature. Normally, this is the cosmic microwave background temperature of 2.7 K, which

has a negligible influence on molecular emission. However, background dust continuum temperatures are significantly higher toward NGC 6334I and it is therefore important to take this effect into account to properly simulate molecular spectra.  $T_{\text{BG}}$  varies for every position and frequency range toward NGC 6334I. Its values are given in Table 1. Due to the extended molecular emission in NGC 6334I and the relatively small beam size, the emission is assumed to be beam filling and thus has a beam filling factor of one.

The analysis of spectral lines is performed under the assumption that molecules are in local thermodynamic equilibrium (LTE) and have a single excitation temperature. The excitation temperature is determined from the observed line brightness temperature ( $\Delta T_{\text{B}}$ ) above the background continuum of optically thick rotational lines and  $T_{\text{BG}}$  following the formalism of Turner (1991) (see also section 2.2.1. of El-Abd et al. 2019). Toward each positions all molecules are thus analyzed with the same excitation temperature. In the first step of the data analysis, rotational lines of a molecule are identified and a by-eye synthetic fit of these lines is made. From the by-eye fit the  $V_{\text{LSR}}$  and  $\Delta V$  are determined, which in most cases yield similar values as given in El-Abd et al. (2019). The errors on both the  $V_{\text{LSR}}$  and  $\Delta V$  are conservatively estimated to be  $\pm 0.3 \text{ km s}^{-1}$ . Then, by cross checking with the spectral line databases, optically thin lines ( $\tau \ll 1$ ) are selected that are free of line blends with other species, although blends in the line wings of other species may occur. CASSIS then performs a regular grid  $\chi^2$  minimization routine on the selected lines, where the column density is given as a free parameter within  $\pm 1$  order of magnitude of the by-eye determined value. The best fit (i.e., lowest  $\chi^2$  value) determines the column density. In most cases, the error on the column density is given by the  $1\sigma$  fit error plus a 10% flux uncertainty. A larger error of 30% is used for  $\text{CH}_3\text{NHCHO}$ , due to higher level of line blending. Further details on the CASSIS line analysis procedure can be found in Ligterink et al. (2018b) and Bøgelund et al. (2019b).

## 3. RESULTS

Except for position MM2-iii, molecular line emission of  $\text{NH}_2\text{CN}$ ,  $\text{HN}^{12}\text{CO}$ ,  $\text{HN}^{13}\text{CO}$ ,  $\text{NH}_2^{12}\text{CHO}$ ,  $\text{NH}_2^{13}\text{CHO}$ , and  $\text{CH}_3\text{C(O)NH}_2$  are detected toward all positions. The detected lines are listed in Table 5. Many of the lines of the main isotopologues of  $\text{HNCO}$  and  $\text{NH}_2\text{CHO}$  are optically thick and therefore not used for further analysis. Following the routine described in section 2.2, the spectra of the remaining molecules were simulated and column densities derived.  $\text{NH}_2\text{CN}$  and

<sup>2</sup> CASSIS has been developed by IRAP-UPS/CNRS (<http://cassis.irap.omp.eu>).

**Table 1.** Physical parameters for spectra analysed toward NGC 6334I

Position	RA	DEC	$V_{\text{LSR}}^{\dagger}$	$\Delta V$	$T_{\text{ex}}$	$T_{\text{BG}}^{\ddagger}$			
						(a)	(b)	(c)	(d)
	hh:mm:ss	dd:mm:ss	(km s <sup>-1</sup> )	(km s <sup>-1</sup> )	(K)				
MM1-i	17:20:53.373	-35.46.58.341	-7.0	3.25	135	10.1	26.9	31.3	31.3
MM1-ii	17:20:53.386	-35.46.57.112	-4.0 – -4.5	3.25	175	38.9	79.7	94.6	85.1
MM1-iii	17:20:53.387	-35.46.57.533	-5.2	3.00	225	50.8	108.2	129.7	120.3
MM1-iv	17:20:53.420	-35.46.59.088	-8.2	3.50	150	15.7	38.4	44.8	73.6
MM1-v	17:20:53.434	-35.46.57.856	-4.4	3.25	285	69.0	159.3	192.7	176
MM1-vi	17:20:53.435	-35.46.58.731	-7.0 – -7.5	3.25	190	30.2	77.6	88.6	94.4
MM1-vii	17:20:53.459	-35.46.57.661	-4.0	3.00	185	43.4	96.5	112.4	106.7
MM1-viii	17:20:53.469	-35.46.58.724	-6.8	3.00	150	25.8	57.1	64.7	81.9
MM1-ix	17:20:53.475	-35.46.57.156	-5.0	2.50	150	16.9	36.8	45.2	65.7
MM1-nmf	17:20:53.461	-35.46.57.284	-4.5	2.50	150	31.1	66.8	80.9	88.1
MM2-i	17:20:53.152	-35.46.59.416	-9.0	2.80	150	9.2	21.8	27.8	57.5
MM2-ii	17:20:53.178	-35.46.59.494	-9.0	2.80	200	17.4	44.4	58.6	98.4
MM2-iii	17:20:53.202	-35.46.59.175	-7.8	2.80	180	18.9	44.2	57.7	76.1

NOTE—<sup>†</sup> For some positions certain molecules are fit with a different  $V_{\text{LSR}}$ . For these cases a  $V_{\text{LSR}}$  range is given. <sup>‡</sup> Four different background temperature values are given for: (a) band 4, (b) band 7 < 300 GHz, (c) band 7 ≥ 300 GHz, and (d) band 10 observations, respectively.

**Table 2.** Summary of Pertinent ALMA Observing Parameters

Parameter	Band 4	Band 7 Low	Band 7 High	Band 10
Project Code	#2017.1.00661.S	#2015.A.00022.T	#2015.A.00022.T	#2017.1.00717.S
Configuration(s)	C43-6	C36-4, C36-5	C36-4, C36-5	C43-3
Primary Beam FWHM (")	41	20	17	6.6
Angular Resolution (") <sup>†</sup>	0.23 × 0.16	0.25 × 0.19	0.22 × 0.17	0.21 × 0.15
Frequency (GHz)	130.03 – 132.02	279.17 – 282.94	336.18 – 339.94	873.88 – 881.33
	144.00 – 145.87	291.18 – 294.94	348.18 – 351.94	890.25 – 897.70
Spectral Resolution (km s <sup>-1</sup> )	1.1	1.1	1.1	0.5
rms (mJy beam <sup>-1</sup> km s <sup>-1</sup> )	0.8	2.0	3.3	44

NOTE—<sup>†</sup> Note that all the observations were convolved to a common synthesized beam size of 0.26" × 0.26".

CH<sub>3</sub>C(O)NH<sub>2</sub> are detected for the first time toward NGC 6334I and their detected spectral lines toward position MM1-i are shown in Figs. 3 and 4. The spectra of the other molecules toward MM1-i and all detections toward MM2-i are presented in Appendix D. The derived column densities toward each position are listed in Table 3. For further analysis, the column densities of HN<sup>12</sup>CO and NH<sub>2</sub><sup>12</sup>CHO are determined from their optically thin <sup>13</sup>C counterparts. To derive the main isotopologue column density, the column densities of the <sup>13</sup>C isotopologues are multiplied with the <sup>12</sup>/<sup>13</sup>C ratio of 62

for NGC 6334I, as determined by Bøgelund et al. (2018), based on equations given by Milam et al. (2005). Moment 0 maps of lines of NH<sub>2</sub>CN, HN<sup>12</sup>CO, NH<sub>2</sub><sup>12</sup>CHO, and CH<sub>3</sub>C(O)NH<sub>2</sub> overplotted on dust continuum contours are shown in Fig. 2.

Toward all positions, spectral features are identified that can be assigned to CH<sub>3</sub>NHCHO, although many of these lines are blended in the wings of other spectral features or on locations where the baseline dips. Despite this, a number of unblended CH<sub>3</sub>NHCHO lines can be identified in the spectra of positions MM1-v, vi,



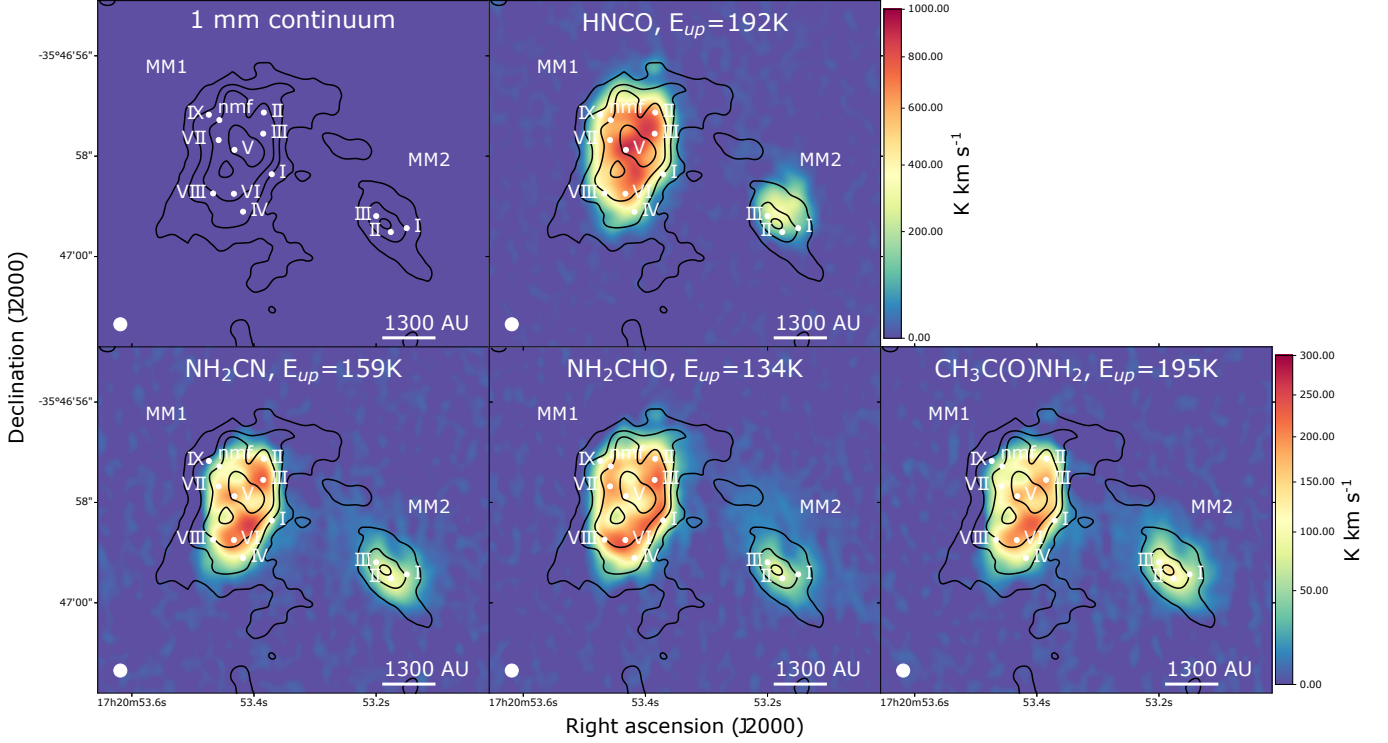


**Figure 2.** Moment 0 maps of  $\text{NH}_2\text{CN}$  (transition:  $14_2\ 13/12 - 13_2\ 12/11$ , 279.821 GHz,  $E_{\text{up}} = 159$  K),  $\text{HNC}$  (transition:  $6_2\ 5/4 - 5_2\ 4/3$ , 131.847 GHz,  $E_{\text{up}} = 192$  K),  $\text{NH}_2\text{CHO}$  (transition:  $15_2\ 14 - 15_1\ 15$ , 281.935 GHz,  $E_{\text{up}} = 159$  K), and  $\text{CH}_3\text{C}(\text{O})\text{NH}_2$  (transition:  $25_{3/2}\ 23 - 24_{2/3}\ 22$ , 279.473 GHz,  $E_{\text{up}} = 195$  K), with 1 mm dust continuum contours overplotted at 17.5, 52.5, 140, and 367.5 mJy beam $^{-1}$ . The angular resolution of the observations (0.26'') is indicated by the bottom left circle. The positions of the extracted spectra are indicated by white dots labeled by capital roman numerals.

vii, and viii and in particular MM1-nmf, which makes it possible to claim the first detection of  $\text{CH}_3\text{NHCHO}$  toward NGC 6334I. The detected  $\text{CH}_3\text{NHCHO}$  lines toward position MM1-nmf are shown in Fig. 5. Figure 13 in Appendix D show the  $\text{CH}_3\text{NHCHO}$  lines in the MM1-nmf spectrum that are present on locations where the baseline dips and thus are not well reproduced by the synthetic spectrum. The spectral features identified toward the other positions in MM1 and in MM2 are insufficient to claim a detection and therefore  $\text{CH}_3\text{NHCHO}$  is tentatively identified toward these positions. Column densities of this species are presented in Table 3.

At a number of positions a handful of spectral features are identified that can be assigned to  $\text{NH}_2\text{C}(\text{O})\text{NH}_2$ . The most and clearest lines are identified toward position MM1-v, see Fig. 6, with at least three unblended lines. While these lines are not enough for a secure detection, a tentative identification can be claimed. The tentative and upper limit column densities of  $\text{NH}_2\text{C}(\text{O})\text{NH}_2$  are presented in Table 3.

#### 4. DISCUSSION

##### 4.1. Chemical comparisons

To get a better understanding of the chemical processes leading to amides, it is useful to compare molecule ratios of the positions within NGC 6334I, but also with other inter- and circumstellar sources. In the following sections molecular ratios with respect to  $\text{NH}_2\text{CHO}$  are discussed. Comparisons are made with the following works: IRAM 30m and Green Bank Telescope (GBT) single dish observations of G+0.693-0.027 (hereafter G+0.693), a quiescent giant molecular cloud (Zeng et al. 2018; Jiménez-Serra et al. 2020), ALMA observations of the incipient hot corino Barnard B1b-S (Marcelino et al. 2018), Northern Extended Millimeter Array (NOEMA) observations of the low-mass protostars SVS13A, NGC 1333-IRAS4A2, NGC 1333-IRAS2A(1) (Coutens et al. 2018; Belloche et al. 2020), ALMA Protostellar Interferometric Line Survey (PILS, Jørgensen et al. 2016) observations of the low-mass protostar IRAS 16293B (Coutens et al. 2016, 2018; Ligtnerink et al. 2018a), GBT and IRAM 30m single dish observations of the galactic center source Sgr B2 (Hollis et al. 2006; Belloche et al. 2013), ALMA observations of the HMSFR Orion KL (Cernicharo et al. 2016), the high-mass star AFGL 4176 (Bøgelund et al. 2019a), and of Sgr B2 (Belloche et al. 2017, 2019). One has to

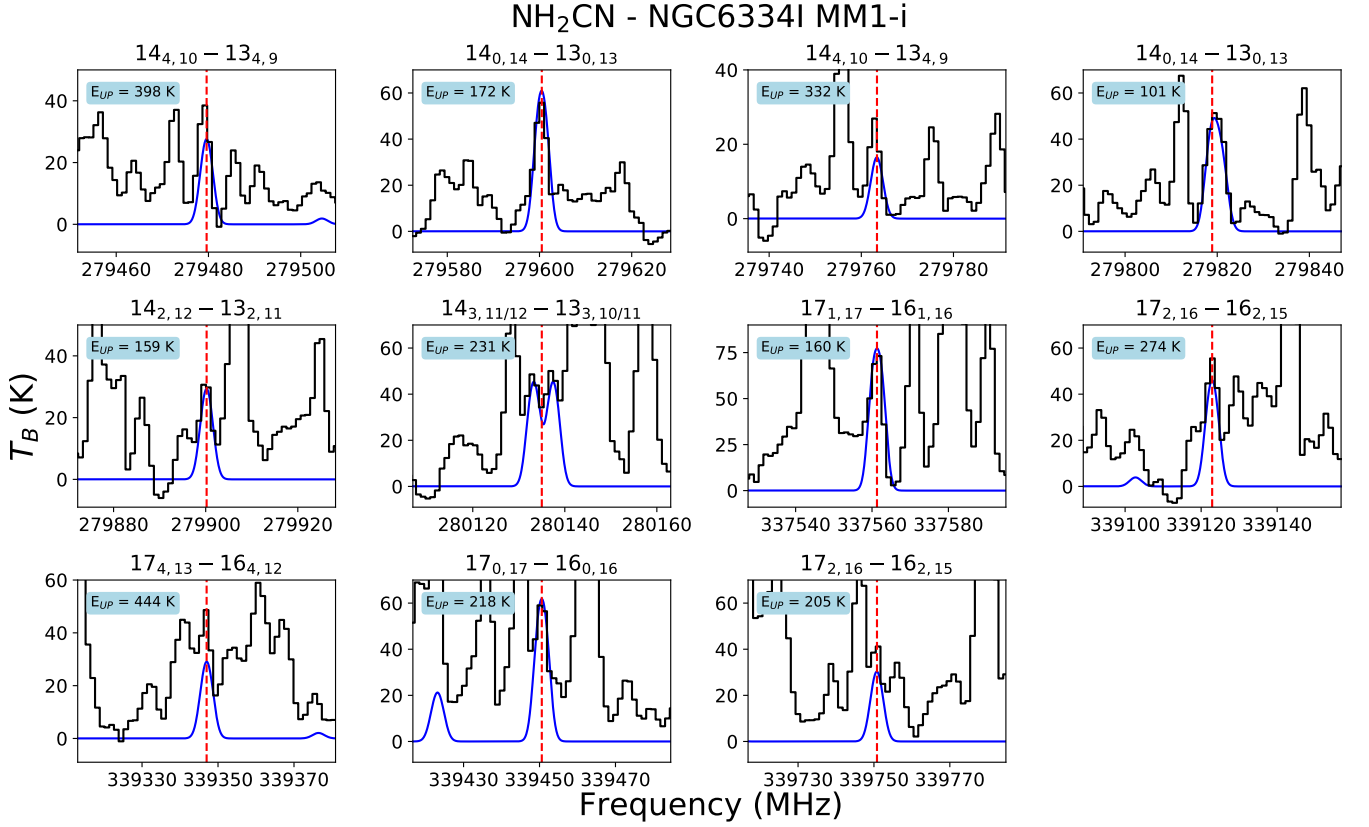


**Figure 3.** Detected transitions of NH<sub>2</sub>CN in the spectrum toward position MM1-i. The observed spectrum is plotted in black, with the synthetic spectrum overplotted in blue and the rest frequency center of the transition is indicated by the red dotted line. The upper state energy of each transition is given in the top left corner.

be aware that precise knowledge of the source size or emitting area of a certain molecule is essential for ratio comparisons. In particular, single dish telescopes do not have the spatial resolution to determine the source size and these are often assumed or estimated, potentially resulting in large column density errors. Finally, mass spectrometric measurements of the Rosetta mission to comet 67P/C-G are used to compare with a Solar System object (Goesmann et al. 2015; Altwegg et al. 2017). The sources are placed in the order: comet 67P, quiescent molecular cloud, low-mass protostars / hot corinos, NGC 6334I, and other HMSFRs, high-mass protostars, and hot cores. The derived ratios are presented in Fig. 7.

#### 4.1.1. Variations in NH<sub>2</sub>CN abundance

Within NGC 6334I, the NH<sub>2</sub>CN over NH<sub>2</sub>CHO ratio shows only minor variations and in general is uniform at  $\sim 1$ -2%. More noticeable is the variation between other sources, which span almost three orders of magnitude. Interestingly, the highest ratios are found for the quiescent molecular cloud and low-mass protostars, while lower ratios are seen in the high-mass sources NGC 6334I and Sgr B2. An important deviation in this pattern is

seen in Orion KL, where  $[\text{NH}_2\text{CN}]/[\text{NH}_2\text{CHO}] = 0.4 - 1.4$  (White et al. 2003, data point not included in Fig. 7). However, it is important to note that the column density of NH<sub>2</sub>CHO in Orion KL was determined using a single spectral line and there is some uncertainty in the assumed excitation temperatures. If this trend is in fact dependent on the source type, it indicates that the source influences either the formation pathway or desorption from grain surfaces of one of the two species.

Recently, Coutens et al. (2018) used chemical models to explain the presence of NH<sub>2</sub>CN toward IRAS 16293-2422B. Chemical networks for this molecule are very sparse, and no plausible gas phase mechanism for its production is currently evident. Coutens et al. (2018) introduced a formation route for NH<sub>2</sub>CN on grain surfaces through the reaction between NH<sub>2</sub> and CN radicals. In their chemical models they determined that this reaction is sensitive to the gas phase H and H<sub>2</sub> density: at high gas densities ( $> 10^9 \text{ cm}^{-3}$ ), hydrogenation of the NH<sub>2</sub> and CN radicals on the ice mantle surface becomes important and the production of NH<sub>2</sub>CN stagnates. Since HMSFRs generally speaking have higher gas densities, this could explain the trend in the observational data

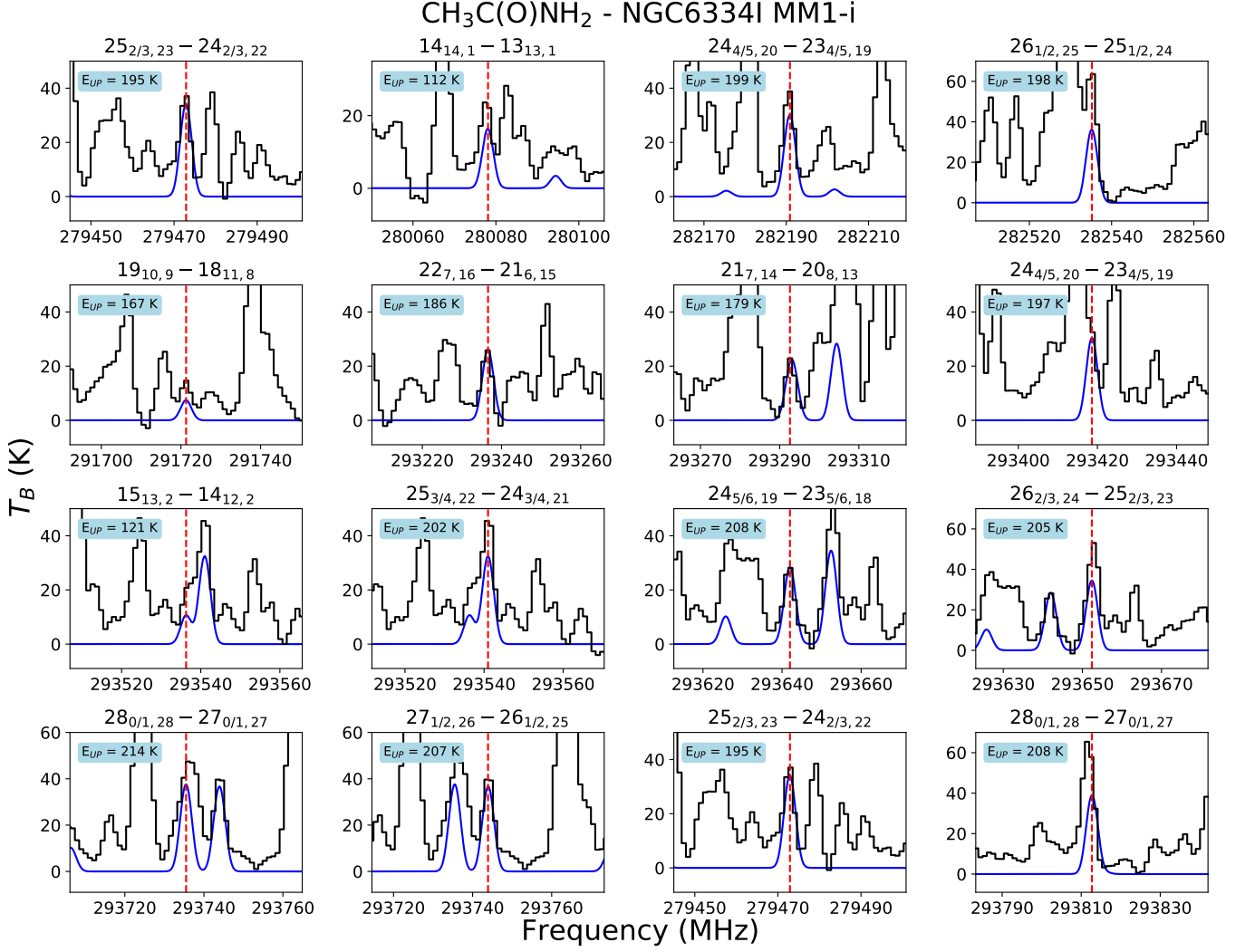
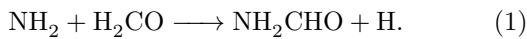


**Figure 4.** Detected transitions of CH<sub>3</sub>C(O)NH<sub>2</sub> in the spectrum toward position MM1-i. The observed spectrum is plotted in black, with the synthetic spectrum overplotted in blue and the rest frequency center of the transition is indicated by the red dotted line. The upper state energy of each transition is given in the top left corner.

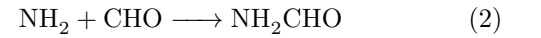
if particular sources enter this density regime for long periods when NH<sub>2</sub>CN might otherwise be forming.

The formation of NH<sub>2</sub>CHO is still a topic of debate, with proponents of both gas phase and solid state ice mantle formation routes (see López-Sepulcre et al. 2019, for an overview of this discussion). Several computational studies have shown that NH<sub>2</sub>CHO can be formed in the gas phase by a near barrierless reaction between NH<sub>2</sub> and H<sub>2</sub>CO (e.g., Barone et al. 2015; Skouteris et al. 2017):

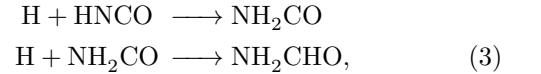


Many studies have been dedicated to understanding the formation of NH<sub>2</sub>CHO in ice mantles, with the main proposed formation routes being the radical reaction be-

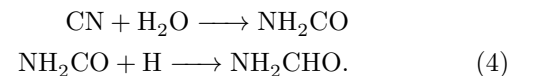
tween NH<sub>2</sub> and CHO directly yielding NH<sub>2</sub>CHO,



and the successive hydrogenation of HNCO (Raunier et al. 2004; Garrod et al. 2008; Jones et al. 2011; Rimola et al. 2018; Enrique-Romero et al. 2019; Haupa et al. 2019):



although experimental work by Noble et al. (2015) indicates that HNCO cannot be hydrogenated. A third option is the reaction of CN radicals with water ice as proposed in theoretical work by Rimola et al. (2018):



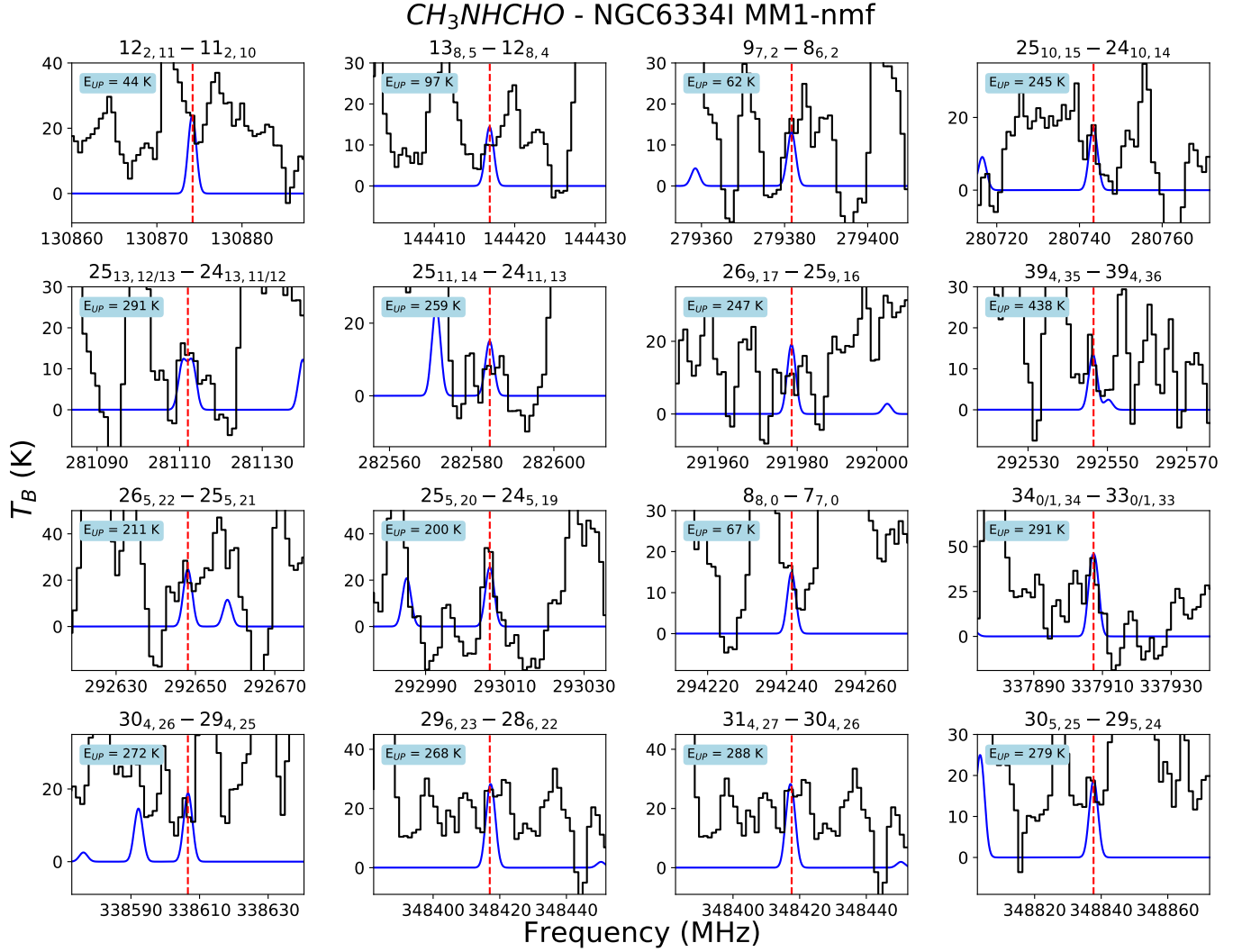
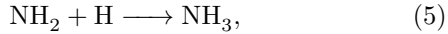


**Figure 5.** Detected transitions of CH<sub>3</sub>NHCHO in the spectrum toward position MM1-nmf. The observed spectrum is plotted in black, with the synthetic spectrum overplotted in blue and the rest frequency center of the transition is indicated by the red dotted line. The upper state energy of each transition is given in the top left corner.

The aforementioned influence of the hydrogen density on the NH<sub>2</sub>CN formation reaction would also be expected to influence NH<sub>2</sub>CHO formation in the ice. Reaction 2 would become less important, instead favoring the hydrogenation of NH<sub>2</sub> to NH<sub>3</sub>:



while at the same time the increased availability of atomic hydrogen could increase the efficiency of Reaction 3, potentially allowing it to dominate. On the other hand, gas phase production of NH<sub>2</sub>CHO can increase under the condition that gas phase NH<sub>2</sub> and H<sub>2</sub>CO densities increase. This can happen as the gas phase density increases from low-mass to high-mass sources. Finally, top-down reaction pathways can contribute to an increased NH<sub>2</sub>CHO column density. For example, radiation interacting with gas phase CH<sub>3</sub>C(O)NH<sub>2</sub> can

produce the NH<sub>2</sub>CO radical, which in turn can produce NH<sub>2</sub>CHO (e.g., Spall & Steacie 1957). If radiation fields increase in strength from low-mass to high-mass sources, such a channel can become prominent and result in a lower [NH<sub>2</sub>CN]/[NH<sub>2</sub>CHO] ratio. However, for larger molecules, such as dipeptides, experiments show that photolysis of these species primarily leads to the breaking of the peptide bond itself, instead of its surrounding bonds (Johns et al. 1968; Neubacher & Schnepel 1977, at conditions not relevant to the interstellar medium). It is therefore questionable whether top-down chemistry can efficiently produce NH<sub>2</sub>CHO (see also section 4.1.2), but dedicated experiments under interstellar conditions are needed to answer this question. In general, care has to be taken with these chemical explanations, as they will influence formation pathways of, and



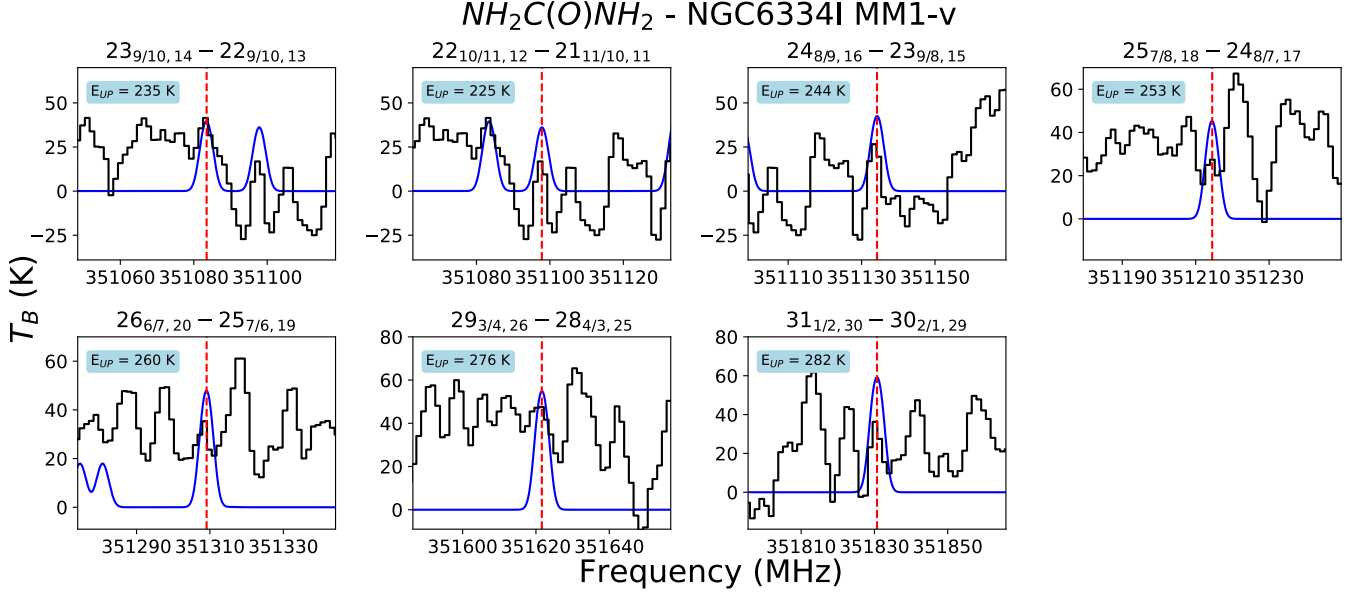


**Figure 6.** Overview of  $\text{NH}_2\text{C}(\text{O})\text{NH}_2$  spectral features toward position MM1-v. The observed spectrum is plotted in black, with the synthetic spectrum overplotted in blue and the rest frequency center of the transition is indicated by the red dotted line. The upper state energy of each transition is given in the top left corner.

**Table 3.** Column densities and upper limits of amides analysed in this work

Position	$T_{\text{ex}}$ (K)	$N(\text{NH}_2\text{CN})$ $\text{cm}^{-2}$	$N(\text{HN}^{13}\text{CO})$ $\text{cm}^{-2}$	$N(\text{NH}_2^{13}\text{CHO})$ $\text{cm}^{-2}$	$N(\text{CH}_3\text{C}(\text{O})\text{NH}_2)$ $\text{cm}^{-2}$	$N(\text{CH}_3\text{NHCHO})$ $\text{cm}^{-2}$	$N(\text{NH}_2\text{C}(\text{O})\text{NH}_2)$ $\text{cm}^{-2}$
MM1-i	135	$(5.9 \pm 0.9) \times 10^{15}$	$(9.9 \pm 3.0) \times 10^{15}$	$(8.6 \pm 1.4) \times 10^{15}$	$(4.7 \pm 0.7) \times 10^{16}$	$\lesssim (7.5 \pm 2.8) \times 10^{16}$	$\leq 2.0 \times 10^{15}$
MM1-ii	175	$(1.8 \pm 0.3) \times 10^{16}$	$(4.5 \pm 1.4) \times 10^{16}$	$(2.2 \pm 0.6) \times 10^{16}$	$(7.4 \pm 1.1) \times 10^{16}$	$\leq 1.5 \times 10^{17}$	$\leq 5.0 \times 10^{15}$
MM1-iii	225	$(3.5 \pm 0.5) \times 10^{16}$	$(6.0 \pm 1.8) \times 10^{16}$	$(3.2 \pm 0.5) \times 10^{16}$	$(1.7 \pm 0.4) \times 10^{17}$	$\leq 2.5 \times 10^{17}$	$\leq 1.0 \times 10^{16}$
MM1-iv	150	$(7.8 \pm 1.6) \times 10^{15}$	$(1.3 \pm 0.2) \times 10^{16}$	$(1.3 \pm 0.2) \times 10^{16}$	$(4.0 \pm 1.2) \times 10^{17}$	$\lesssim (1.0 \pm 0.4) \times 10^{17}$	$\leq 1.0 \times 10^{16}$
MM1-v	285	$(4.0 \pm 0.4) \times 10^{16}$	$(1.2 \pm 0.1) \times 10^{17}$	$(2.7 \pm 0.3) \times 10^{16}$	$(2.3 \pm 0.2) \times 10^{17}$	$(3.6 \pm 0.7) \times 10^{17}$	$\lesssim (5.0 \pm 2.0) \times 10^{16}$
MM1-vi	190	$(2.6 \pm 0.6) \times 10^{16}$	$(3.7 \pm 0.5) \times 10^{16}$	$(2.8 \pm 0.3) \times 10^{16}$	$(1.6 \pm 0.2) \times 10^{17}$	$(2.0 \pm 0.6) \times 10^{17}$	$\leq 1.0 \times 10^{16}$
MM1-vii	185	$(1.6 \pm 0.3) \times 10^{16}$	$(4.4 \pm 0.5) \times 10^{16}$	$(3.8 \pm 0.4) \times 10^{16}$	$(1.6 \pm 0.2) \times 10^{17}$	$(2.0 \pm 0.6) \times 10^{17}$	$\leq 3.0 \times 10^{16}$
MM1-viii	150	$(7.8 \pm 0.8) \times 10^{16}$	$(2.0 \pm 0.3) \times 10^{16}$	$(1.6 \pm 0.3) \times 10^{16}$	$(7.1 \pm 1.1) \times 10^{16}$	$(1.4 \pm 0.5) \times 10^{17}$	$\leq 2.0 \times 10^{16}$
MM1-ix	150	$(2.3 \pm 0.4) \times 10^{15}$	$(6.4 \pm 1.3) \times 10^{15}$	$(4.8 \pm 0.5) \times 10^{15}$	$(1.6 \pm 0.3) \times 10^{16}$	$\lesssim (4.8 \pm 1.5) \times 10^{16}$	$\leq 1.5 \times 10^{16}$
MM1-nmf	150	$(1.1 \pm 0.2) \times 10^{16}$	$(1.9 \pm 0.3) \times 10^{16}$	$(1.6 \pm 0.3) \times 10^{16}$	$(6.8 \pm 1.3) \times 10^{16}$	$(1.0 \pm 0.5) \times 10^{17}$	$\leq 1.0 \times 10^{16}$
MM2-i	150	$(3.5 \pm 0.6) \times 10^{15}$	$(1.4 \pm 0.5) \times 10^{16}$	$(3.3 \pm 1.0) \times 10^{15}$	$(5.9 \pm 1.6) \times 10^{16}$	$\leq 5.0 \times 10^{16}$	$\leq 3.0 \times 10^{15}$
MM2-ii	200	$(4.0 \pm 0.5) \times 10^{15}$	$(2.3 \pm 0.7) \times 10^{16}$	$(3.8 \pm 1.1) \times 10^{15}$	$(8.8 \pm 1.6) \times 10^{16}$	$\leq 6.0 \times 10^{16}$	$\leq 4.0 \times 10^{15}$

ratios between, other species as well. Yet, trends like  $[\text{NH}_2\text{CN}]/[\text{NH}_2\text{CHO}]$  are not observed for most other species, such as  $\text{HNCO}$  and  $\text{CH}_3\text{C}(\text{O})\text{NH}_2$ , see Fig. 7.

Alternatively, the ice mantle desorption characteristics can explain the observed trend. Thermal desorption depends on the binding energy of the molecule. Recent laboratory studies using temperature programmed desorption investigated the binding energy of  $\text{NH}_2\text{CHO}$  on graphite and on amorphous water deposited onto

graphite (Chaabouni et al. 2018). In the latter case,  $\text{NH}_2\text{CHO}$  remained on the surface until after the water had already desorbed. Those authors found binding energies of 4810 and 5056–6990 K for amorphous water and for formamide, respectively (assuming a desorption-rate prefactor of  $10^{12} \text{ s}^{-1}$ ); the binding energy for  $\text{NH}_2\text{CHO}$  corresponds simply to binding to the graphite left behind following the desorption of the water. The desorption energy of  $\text{NH}_2\text{CN}$  is not experimentally determined,

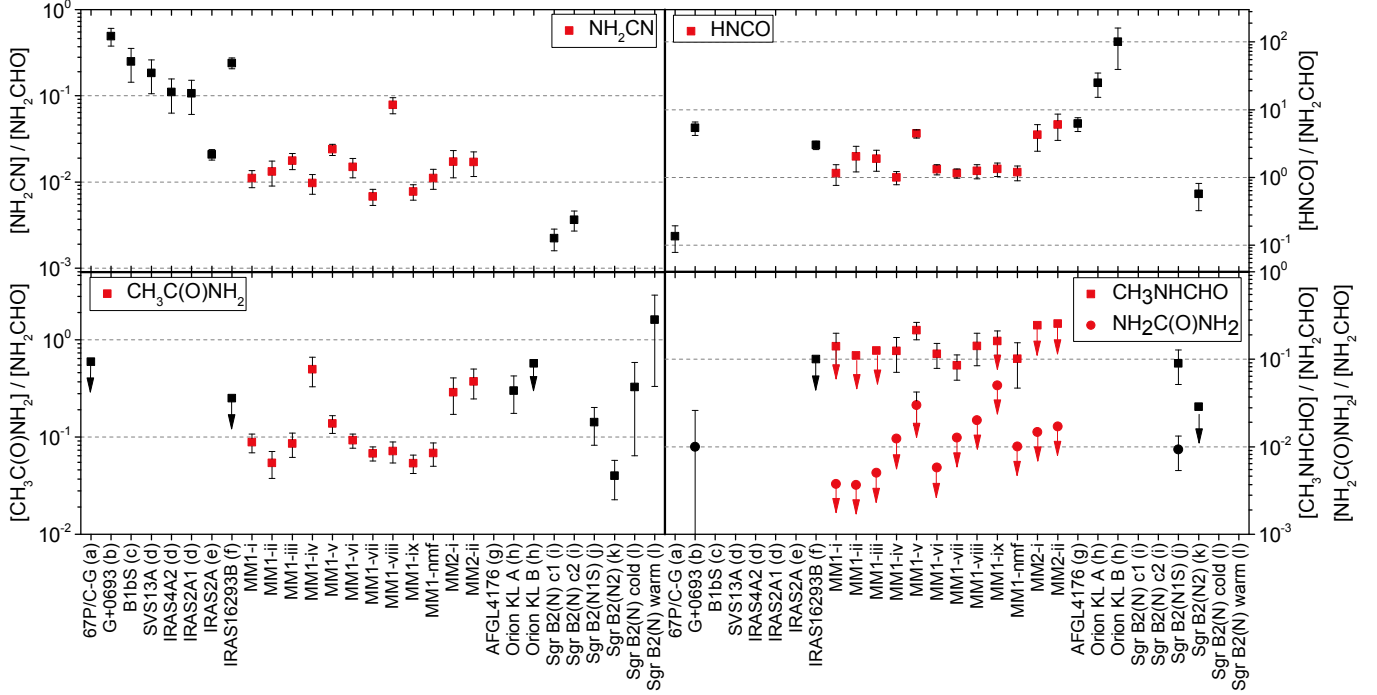


**Figure 7.** Column density ratios of  $\text{NH}_2\text{CN}$  (top left),  $\text{HNCO}$  (top right),  $\text{CH}_3\text{C}(\text{O})\text{NH}_2$  (bottom left), and  $\text{CH}_3\text{NHCHO}$  and  $\text{NH}_2\text{C}(\text{O})\text{NH}_2$  (bottom right) with respect to  $\text{NH}_2\text{CHO}$ . Ratios for NGC 6334I MM1 and MM2 are indicated in red. For the NGC 6334I data,  $^{13}\text{C}$  isotopes of  $\text{HNCO}$  and  $\text{NH}_2\text{CHO}$  are used, multiplied by the  $^{12}/^{13}\text{C}$  ratio of 62. The sources are placed in the order: comet 67P, quiescent molecular cloud, low-mass protostars / hot corinos, NGC 6334I, and other HMSFRs, high-mass protostars, and hot cores. Data are taken from: <sup>a</sup>Goesmann et al. (2015); <sup>b</sup>Altwegg et al. (2017), <sup>c</sup>Zeng et al. (2018); <sup>d</sup>Jiménez-Serra et al. (2020), <sup>e</sup>Marcelino et al. (2018), <sup>f</sup>Belloche et al. (2020), <sup>g</sup>Coutens et al. (2018), <sup>h</sup>Coutens et al. (2016, 2018); <sup>i</sup>Ligterink et al. (2018a), <sup>j</sup>Bøgelund et al. (2019a), <sup>k</sup>Cernicharo et al. (2016), <sup>l</sup>Belloche et al. (2013), <sup>m</sup>Belloche et al. (2017), <sup>n</sup>Belloche et al. (2019), and <sup>o</sup>Hollis et al. (2006).

but chemical models commonly use binding energies of 5556 K for both species, based on the interpolation method described by Garrod & Herbst (2006). If the true value for  $\text{NH}_2\text{CN}$  were close to or less than the binding energy of water, or otherwise much less than that of  $\text{NH}_2\text{CHO}$ , it could influence the  $[\text{NH}_2\text{CN}]/[\text{NH}_2\text{CHO}]$  trend. When a source is sufficiently warm over a large area, such as a HMSFR, most volatile organic species will desorb from the grains. However, a more compact source, such as a single low-mass protostar, will have a decreasing radial temperature profile. Around such sources, species with a low desorption energy desorb over a larger area than those with a high desorption energy. Depending on the spatial resolution of the observations, the beam may simply cover a larger emitting area of  $\text{NH}_2\text{CN}$  than of  $\text{NH}_2\text{CHO}$ , thus explaining the decreasing ratio. To better understand how desorption characteristics influence the  $[\text{NH}_2\text{CN}]/[\text{NH}_2\text{CHO}]$  ratio, laboratory measurements of the  $\text{NH}_2\text{CN}$  desorption energy are required, but non-thermal desorption processes of  $\text{NH}_2\text{CN}$  and  $\text{NH}_2\text{CHO}$ , such as reactive desorption and photodesorption, need to be studied as well.

#### 4.1.2. *HNCO chemistry*

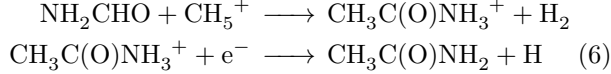
For many years, an abundance correlation between  $\text{HNCO}$  and  $\text{NH}_2\text{CHO}$  has been observed toward a large range of interstellar sources, which has led to the belief that there is a direct chemical relationship between these two species (see López-Sepulcre et al. 2019, for a recent review). In Fig. 7, the  $[\text{HNCO}]/[\text{NH}_2\text{CHO}]$  ratios found toward NGC 6334I are compared with ratios from a select number of other sources. We note that the  $\text{HNCO}$  column density is determined from its  $^{13}\text{C}$  isotope, multiplied by a  $^{12}/^{13}\text{C}$  ratio of 62. In NGC 6334I MM1 the  $[\text{HNCO}]/[\text{NH}_2\text{CHO}]$  is slightly above one, while in MM2 it is somewhat higher at a ratio of  $\sim 5$ . Therefore, the ratios in NGC 6334I follows the average interstellar trend and strengthens the probable link between  $\text{HNCO}$  and  $\text{NH}_2\text{CHO}$ . Whether this is a direct chemical link (e.g., Raunier et al. 2004; Haupa et al. 2019) or an effect caused by similar chemical responses to physical conditions (Quénard et al. 2018) cannot be inferred from these ratios. Since  $\text{HNCO}$  and  $\text{CH}_3\text{C}(\text{O})\text{NH}_2$  are found co-spatially toward NGC 6334I, gas phase ion-molecule destruction of  $\text{CH}_3\text{C}(\text{O})\text{NH}_2$  may be to some extent re-

sponsible for the observed abundances of HNCO, as was suggested by Garrod et al. (2008) and Tideswell et al. (2010). In aforementioned works,  $\text{CH}_3\text{C}(\text{O})\text{NH}_2$  forms by radical-radical reactions on grain surfaces, together with  $\text{NH}_2\text{CHO}$ , where after it is released to the gas phase and can be destroyed by ions. This pathway therefore provides an indirect link between HNCO and  $\text{NH}_2\text{CHO}$ , by way of  $\text{CH}_3\text{C}(\text{O})\text{NH}_2$  and other larger amides, assuming that  $\text{NH}_2\text{CHO}$  and larger amides form in related reactions in ice mantles. This mechanism can help explain the higher  $[\text{HNCO}] / [\text{NH}_2\text{CHO}]$  ratio in MM2, if more ions are present in MM2, for example due to a stronger radiation field, which result in enhanced HNCO production.

#### 4.1.3. The large amides

Of the large amides,  $\text{CH}_3\text{C}(\text{O})\text{NH}_2$  is detected toward most positions. A relatively small abundance difference is seen between MM1 and MM2, but in general ratios are quite similar throughout the region. This suggests that production of  $\text{CH}_3\text{C}(\text{O})\text{NH}_2$  is occurring through a similar mechanism throughout the region.

Various gas phase formation routes of  $\text{CH}_3\text{C}(\text{O})\text{NH}_2$  have been proposed and computationally tested (Hollis et al. 2006; Quan & Herbst 2007; Halfen et al. 2011; Redondo et al. 2014), with the reaction



considered to be the most efficient. In ice mantles, however,  $\text{CH}_3\text{C}(\text{O})\text{NH}_2$  is thought (e.g., Agarwal et al. 1985; Ligterink et al. 2018a) to be primarily produced by Reaction 7:



Laboratory simulations of chemical reactions in ice mantles of interstellar dust grains found a  $[\text{CH}_3\text{C}(\text{O})\text{NH}_2]/[\text{NH}_2\text{CHO}]$  ratio of 0.4 upon desorption from the surface (Ligterink et al. 2018a), close to the observed average of  $\sim 0.15$  in NGC 6334I. Ice formation of  $\text{CH}_3\text{C}(\text{O})\text{NH}_2$ , in particular during the dense cloud stage of star formation, is a plausible mechanism to explain its uniform ratio derived throughout NGC 6334I. While abundances also seem to be similar between NGC 6334I and other sources, it is too early to say if the general interstellar  $\text{CH}_3\text{C}(\text{O})\text{NH}_2$  chemistry is the result of the same process(es). A larger sample with confirmed detections and better constraints on the source sizes of the emitting regions toward these objects is required.

Both  $\text{CH}_3\text{C}(\text{O})\text{NH}_2$  and  $\text{CH}_3\text{NHCHO}$  are present at  $\sim 10\%$  with respect to  $\text{NH}_2\text{CHO}$  toward NGC 6334I.

This similarity in abundances supports the conclusion of Belloche et al. (2017) that kinetic processes are at the basis of the formation of these species rather than thermal equilibrium. This species can form by energetically processing frozen  $\text{CH}_3\text{NH}_2\text{:CO}$  mixtures (Frigge et al. 2018) and thus can be formed on interstellar dust grains. We note that  $\text{CH}_3\text{NH}_2$  is abundantly present toward NGC 6334I (Bøgelund et al. 2019b).  $\text{CH}_3\text{NHCHO}$  abundances are similar between NGC 6334I and Sgr B2(N1S), the only other source where this molecule is securely detected (Belloche et al. 2019). However, compared to a tentative identification toward Sgr B2(N2), a difference of almost an order of magnitude is seen. At this point it not possible to draw any conclusions on the overall interstellar chemistry of  $\text{CH}_3\text{NHCHO}$  and more observations of this molecule are required.

The ratios of the tentative detection and upper limits of  $\text{NH}_2\text{C}(\text{O})\text{NH}_2$  vary about an order of magnitude within NGC 6334I. It is possible that high temperatures are needed to desorb  $\text{NH}_2\text{C}(\text{O})\text{NH}_2$  from dust grains, thus causing this variation. We note that this molecule is tentatively detected toward position MM1-v, which has the highest excitation temperature, and perhaps physical temperature, of 285 K. Compared to secure detections of  $\text{NH}_2\text{C}(\text{O})\text{NH}_2$  toward Sgr B2(N1S) and G+0.693 (Belloche et al. 2019; Jiménez-Serra et al. 2020), abundances seem to be similar at the few percent level. However, as with the case of  $\text{CH}_3\text{NHCHO}$ , it is too early to draw conclusions about the formation of  $\text{NH}_2\text{C}(\text{O})\text{NH}_2$  at this stage. The tentative identification of  $\text{NH}_2\text{C}(\text{O})\text{NH}_2$  warrants future searches for this molecule toward NGC 6334I in order to securely detect this species, better constrain its abundance, and refine and constrain chemical models to elucidate its chemistry.

#### 4.2. Implications for biomolecule formation

The detection of  $\text{CH}_3\text{C}(\text{O})\text{NH}_2$  and tentative identification of  $\text{CH}_3\text{NHCHO}$  in NGC 6334I strengthens the case that these molecules can contribute to the formation of biomolecules. It is possible that, in the interstellar medium, these molecules act as precursor species to, or form in parallel with, larger biomolecules. Multiple laboratory experiments show that in UV irradiated simulated ice mantles, consisting of simple molecules such as  $\text{H}_2\text{O}$ ,  $\text{NH}_3$ ,  $\text{CH}_3\text{OH}$ , and  $\text{CH}_4$ , simple amides and molecules of greater complexity, including biomolecules, form simultaneously (e.g., Agarwal et al. 1985; Caro et al. 2002; Caro & Schutte 2003; Nuevo et al. 2010; Ligterink et al. 2018a; Oba et al. 2019). If the formation of amides in the interstellar medium primarily occurs on interstellar dust grains, it is not unlikely that biomolecules are present as well, at least on grain sur-

faces. Their presence and abundance in the gas phase depends on the local physical conditions and parameter such as binding energy and photodissociation rate.

Alternatively, amides can also be involved in the earliest stages of biochemistry after delivery to a newly formed planet. Under early Earth conditions and catalyzed by minerals, metals, or clays,  $\text{NH}_2\text{CHO}$  can form a variety of biomolecules, most notably nucleobases and amino acids (Saladino et al. 2012, and references therein). Cyanamide and carbamide are known to act as condensing agents in amino acids and nucleotide polymerization reactions (Ibanez et al. 1971; Sakurai & Yanagawa 1984). It is not unlikely that  $\text{CH}_3\text{C}(\text{O})\text{NH}_2$  and  $\text{CH}_3\text{NHCHO}$  engage in similar reactions, but laboratory investigations on this topic are limited.

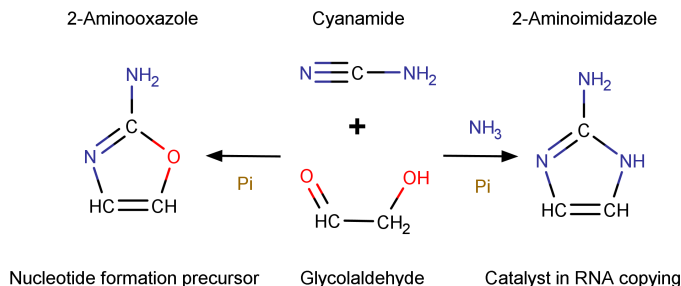


**Figure 8.** Reactions involving the interstellar molecules  $\text{NH}_2\text{CN}$  and  $\text{CH}_2(\text{OH})\text{CHO}$ . In a liquid water environment and catalyzed by inorganic phosphates ( $\text{P}_i$ ), either 2-aminooxazole (left), a nucleotide precursor, or, when  $\text{NH}_3$  is added, 2-aminoimidazole (right), a catalyst for RNA copying, is formed. Figure adopted from Fahrenbach et al. (2017).

The cocktail of molecules found toward NGC 6334I, but also other sources such as the sun-like protostar IRAS 16293B, presents more options to directly form biomolecules on a young Earth. This is highlighted by the reaction between  $\text{NH}_2\text{CN}$  and glycolaldehyde ( $\text{HC}(\text{O})\text{CH}_2\text{OH}$ ), resulting in either 2-aminooxazole or 2-aminoimidazole, a precursor to nucleotide formation and a catalyst for RNA copying, respectively (see Figure 8, Patel et al. 2015; Fahrenbach et al. 2017). In aforementioned works, both  $\text{NH}_2\text{CN}$  and  $\text{HC}(\text{O})\text{CH}_2\text{OH}$  are part of *in-situ* chemistry on a planetary body (Earth in this case) deriving from HCN and involve multiple reaction steps to produce these species. Formation of these two species in space and subsequent delivery to a young Earth directly supplies the *in-situ* chemical network with these compounds, leading to a more rapid emergence of biomolecules.

## 5. CONCLUSION

In this work, a group of amides is analysed toward the high-mass star-forming region NGC 6334I. Secure detections of  $\text{NH}_2\text{CN}$ ,  $\text{HNCO}$ ,  $\text{NH}_2\text{CHO}$ ,  $\text{CH}_3\text{C}(\text{O})\text{NH}_2$ , and  $\text{CH}_3\text{NHCHO}$  are presented along with a tentative identification of  $\text{NH}_2\text{C}(\text{O})\text{NH}_2$ . Abundances of amides are determined with respect to  $\text{NH}_2\text{CHO}$  and are generally found to be similar within NGC 6334I, often varying less than a factor of five, hinting that the same chemical pathways and physical conditions are at the basis of this chemistry, despite the large size and physical differences of this HMSFR. It is plausible that production of these amides occurred on surfaces of interstellar dust grains during the dense cloud stage of the star formation process in NGC 6334I. The relatively minor abundance variations between MM1 and MM2 can be the result of slightly different physical conditions, such as higher radiation fields, resulting in the efficient photodestruction of one or more of the amides, either in the ice mantles or gas phase.

The comparison of (tentative) abundances of  $\text{CH}_3\text{C}(\text{O})\text{NH}_2$ ,  $\text{CH}_3\text{NHCHO}$ , and  $\text{NH}_2\text{C}(\text{O})\text{NH}_2$  in NGC 6334I with abundances of these species toward other sources shows that these are quite similar. This hints that similar processes may be responsible for the formation of these species, but due to the limited number of detections and different observing parameters, it is too early to draw any strong conclusion. A different trend is observed for  $[\text{NH}_2\text{CN}] / [\text{NH}_2\text{CHO}]$ , for which abundances vary three orders of magnitude over a large number of observed sources. This variation seems to depend on the source type, with high ratios toward low-mass and pre-stellar sources and low ratios toward high-mass sources. The origin of this variation is not easily explained and could depend on different reaction pathways and physical conditions, and is perhaps affected by observational parameters as well. More experimental and theoretical work is needed to confirm this. However, it is likely that  $\text{NH}_2\text{CN}$  is not part of the same chemistry that produces the other amides. The rich amide chemistry toward NGC 6334I, in combination with other molecules, such as  $\text{HC}(\text{O})\text{CH}_2\text{OH}$ , strengthens the case that interstellar molecules contribute to the rapid emergence of biomolecules on planetary objects.

## ACKNOWLEDGMENTS

We thank Dr. E.G. Bøgelund for helpful discussions and support in the data analysis. This paper makes use of the following ALMA data: ADS/JAO.ALMA#2017.1.00717.S, #2017.1.00661.S, and #2015.A.00022.T. ALMA is a partnership of ESO (representing its member states), NSF (USA) and NINS (Japan), together with NRC (Canada) and NSC and ASIAA (Taiwan) and KASI (Republic of Korea), in cooperation with the Republic of Chile. The Joint ALMA Observatory is operated by ESO, AUI/NRAO and NAOJ. The National Radio Astronomy Observatory is a facility of the National Science Foundation operated under cooperative agreement by Associated Universities, Inc. Support for B.A.M. was provided by NASA through Hubble Fellowship grant #HST-HF2-51396 awarded by the Space Telescope Science Institute, which is operated by the Association of Universities for Research in Astronomy, Inc., for NASA, under contract NAS5-26555. This research made use of NASA's Astrophysics Data System Bibliographic Services, Astropy, a community-developed core Python package for Astronomy, and APLpy, an open-source plotting package for Python hosted at <http://aplpy.github.com>.

## REFERENCES

- Agarwal, V., Schutte, W., Greenberg, J., et al. 1985, *Origins of Life and Evolution of the Biosphere*, 16, 21
- Altwegg, K., Balsiger, H., Berthelier, J.-J., et al. 2017, *Monthly Notices of the Royal Astronomical Society*, 469, S130
- Barone, V., Latouche, C., Skouteris, D., et al. 2015, *Monthly Notices of the Royal Astronomical Society: Letters*, 453, L31
- Belloche, A., Garrod, R. T., Müller, H. S. P., et al. 2019, *A&A*, 628, A10, doi: [10.1051/0004-6361/201935428](https://doi.org/10.1051/0004-6361/201935428)
- Belloche, A., Müller, H. S., Menten, K. M., Schilke, P., & Comito, C. 2013, *Astronomy & Astrophysics*, 559, A47
- Belloche, A., Meshcheryakov, A. A., Garrod, R. T., et al. 2017, *A&A*, 601, A49, doi: [10.1051/0004-6361/201629724](https://doi.org/10.1051/0004-6361/201629724)
- Belloche, A., Maury, A., Maret, S., et al. 2020, *Astronomy & Astrophysics*
- Blanco, S., López, J. C., Lesarri, A., & Alonso, J. L. 2006, *Journal of the American Chemical Society*, 128, 12111
- Bøgelund, E. G., Barr, A. G., Taquet, V., et al. 2019a, *A&A*, 628, A2, doi: [10.1051/0004-6361/201834527](https://doi.org/10.1051/0004-6361/201834527)
- Bøgelund, E. G., McGuire, B. A., Hogerheijde, M. R., van Dishoeck, E. F., & Ligterink, N. F. W. 2019b, *A&A*, 624, A82, doi: [10.1051/0004-6361/201833676](https://doi.org/10.1051/0004-6361/201833676)
- Bøgelund, E. G., McGuire, B. A., Ligterink, N. F. W., et al. 2018, *A&A*, 615, A88, doi: [10.1051/0004-6361/201832757](https://doi.org/10.1051/0004-6361/201832757)
- Brogan, C., Hunter, T., Cyganowski, C., et al. 2018, *The Astrophysical Journal*, 866, 87
- Brogan, C. L., Hunter, T. R., Cyganowski, C. J., et al. 2016, *ApJ*, 832, 187, doi: [10.3847/0004-637X/832/2/187](https://doi.org/10.3847/0004-637X/832/2/187)
- Brown, R., Godfrey, P., & Storey, J. 1975, *Journal of Molecular Spectroscopy*, 58, 445
- Caro, G. M., & Schutte, W. 2003, *Astronomy & Astrophysics*, 412, 121
- Caro, G. M., Meierhenrich, U., Schutte, W., et al. 2002, *Nature*, 416, 403
- Cernicharo, J., Kisiel, Z., Tercero, B., et al. 2016, *Astronomy & Astrophysics*, 587, L4
- Chaabouni, H., Diana, S., Nguyen, T., & Dulieu, F. 2018, *Astronomy & Astrophysics*, 612, A47
- Chyba, C. F., Thomas, P. J., Brookshaw, L., & Sagan, C. 1990, *Science*, 249, 366
- Coutens, A., Jørgensen, J. K., Van der Wiel, M. H. D., et al. 2016, *Astronomy & Astrophysics*, 590, L6
- Coutens, A., Willis, E., Garrod, R., et al. 2018, *Astronomy & Astrophysics*, 612, A107



- Dukes, D., & Krumholz, M. R. 2012, *The Astrophysical Journal*, 754, 56
- El-Abd, S. J., Brogan, C. L., Hunter, T. R., et al. 2019, *ApJ*, 883, 129, doi: [10.3847/1538-4357/ab3646](https://doi.org/10.3847/1538-4357/ab3646)
- Enrique-Romero, J., Rimola, A., Ceccarelli, C., et al. 2019, *ACS Earth and Space Chemistry*, 3, 2158
- Fahrenbach, A. C., Giurciu, C., Tam, C. P., et al. 2017, *Journal of the American Chemical Society*, 139, 8780
- Frigge, R., Zhu, C., Turner, A. M., et al. 2018, *The Astrophysical Journal*, 862, 84
- Gardner, F., Godfrey, P., & Williams, D. 1980, *Monthly Notices of the Royal Astronomical Society*, 193, 713
- Garrod, R. T., & Herbst, E. 2006, *Astronomy & Astrophysics*, 457, 927
- Garrod, R. T., Weaver, S. L. W., & Herbst, E. 2008, *The Astrophysical Journal*, 682, 283
- Goesmann, F., Rosenbauer, H., Bredehöft, J. H., et al. 2015, *Science*, 349, aab0689
- Halfen, D., Ilyushin, V. V., & Ziurys, L. M. 2015, *The Astrophysical Journal Letters*, 812, L5
- Halfen, D. T., Ilyushin, V., & Ziurys, L. M. 2011, *ApJ*, 743, 60, doi: [10.1088/0004-637X/743/1/60](https://doi.org/10.1088/0004-637X/743/1/60)
- Haupa, K. A., Tarczay, G., & Lee, Y.-P. 2019, *Journal of the American Chemical Society*, 141, 11614
- Hirota, E., Sugisaki, R., Nielsen, C. J., & Sørensen, G. O. 1974, *Journal of Molecular Spectroscopy*, 49, 251
- Hocking, W., Gerry, M., & Winnewisser, G. 1975, *Canadian Journal of Physics*, 53, 1869
- Hollis, J. M., Lovas, F. J., Remijan, A. J., et al. 2006, *ApJL*, 643, L25, doi: [10.1086/505110](https://doi.org/10.1086/505110)
- Hunter, T. R., Brogan, C. L., MacLeod, G., et al. 2017, *The Astrophysical Journal Letters*, 837, L29
- Ibanez, J., Kimball, A., & Oro, J. 1971, *Science*, 173, 444
- Ilyushin, V. V., Alekseev, E. A., Dyubko, S. F., Kleiner, I., & Hougen, J. T. 2004, *Journal of Molecular Spectroscopy*, 227, 115, doi: [10.1016/j.jms.2004.05.014](https://doi.org/10.1016/j.jms.2004.05.014)
- Jiménez-Serra, I., Martín-Pintado, J., Rivilla, V. M., et al. 2020, *arXiv preprint arXiv:2004.07834*
- Johns, R., Looney, F., & Whelan, D. 1968, *Photochemistry and photobiology*, 7, 65
- Jones, B. M., Bennett, C. J., & Kaiser, R. I. 2011, *The Astrophysical Journal*, 734, 78
- Jørgensen, J. K., Van der Wiel, M. H. D., Coutens, A., et al. 2016, *Astronomy & Astrophysics*, 595, A117
- Kahane, C., Ceccarelli, C., Faure, A., & Caux, E. 2013, *The Astrophysical Journal Letters*, 763, L38
- Kasten, W., & Dreizler, H. 1986, *Zeitschrift für Naturforschung A*, 41, 1173
- Kretschmer, U., Consalvo, D., Knaack, A., et al. 1996, *Molecular Physics*, 87, 1159
- Kryvda, A., Gerasimov, V., Dyubko, S., Alekseev, E., & Motiyenko, R. 2009, *Journal of Molecular Spectroscopy*, 254, 28
- Kukolich, S. G., & Nelson, A. 1971, *Chemical Physics Letters*, 11, 383
- Kukolich, S. G., Nelson, A., & Yamanashi, B. 1971, *Journal of the American Chemical Society*, 93, 6769
- Lapinov, A., Golubiatnikov, G. Y., Markov, V., & Guarnieri, A. 2007, *Astronomy Letters*, 33, 121
- Ligterink, N., Terwisscha van Scheltinga, J., Taquet, V., et al. 2018a, *Monthly Notices of the Royal Astronomical Society*, 480, 3628
- Ligterink, N., Coutens, A., Kofman, V., et al. 2017, *Monthly Notices of the Royal Astronomical Society*, 469, 2219
- Ligterink, N. F. W., Calcutt, H., Coutens, A., et al. 2018b, *Astronomy & Astrophysics*, 619, A28
- López-Sepulcre, A., Balucani, N., Ceccarelli, C., et al. 2019, *arXiv e-prints*, arXiv:1909.11770, <https://arxiv.org/abs/1909.11770>
- López-Sepulcre, A., Jaber, A. A., Mendoza, E., et al. 2015, *Monthly Notices of the Royal Astronomical Society*, 449, 2438
- Marcelino, N., Gerin, M., Cernicharo, J., et al. 2018, *Astronomy & Astrophysics*, 620, A80
- McGuire, B. A., Shingledecker, C. N., Willis, E. R., et al. 2017, *ApJL*, 851, L46, doi: [10.3847/2041-8213/aaa0c3](https://doi.org/10.3847/2041-8213/aaa0c3)
- McGuire, B. A., Brogan, C. L., Hunter, T. R., et al. 2018, *ApJL*, 863, L35, doi: [10.3847/2041-8213/aad7bb](https://doi.org/10.3847/2041-8213/aad7bb)
- Milam, S. N., Savage, C., Brewster, M. A., Ziurys, L. M., & Wyckoff, S. 2005, *ApJ*, 634, 1126, doi: [10.1086/497123](https://doi.org/10.1086/497123)
- Moskienko, E., & Dyubko, S. 1991, *Radiophysics and quantum electronics*, 34, 181
- Motiyenko, R., Tercero, B., Cernicharo, J., & Margulès, L. 2012, *Astronomy & Astrophysics*, 548, A71
- Müller, H. S., Schlöder, F., Stutzki, J., & Winnewisser, G. 2005, *Journal of Molecular Structure*, 742, 215
- Müller, H. S., Thorwirth, S., Roth, D., & Winnewisser, G. 2001, *Astronomy & Astrophysics*, 370, L49
- Neubacher, H., & Schnepel, G. H. 1977, *Radiation research*, 72, 48
- Niedenhoff, M., Yamada, K., Belov, S., & Winnewisser, G. 1995, *Journal of Molecular Spectroscopy*, 174, 151
- Noble, J., Theule, P., Congiu, E., et al. 2015, *Astronomy & Astrophysics*, 576, A91
- Nuevo, M., Bredehöft, J. H., Meierhenrich, U. J., d'Hendecourt, L., & Thiemann, W. H.-P. 2010, *Astrobiology*, 10, 245
- Oba, Y., Takano, Y., Naraoka, H., Watanabe, N., & Kouchi, A. 2019, *Nature communications*, 10, 1

- Patel, B. H., Percivalle, C., Ritson, D. J., Duffy, C. D., & Sutherland, J. D. 2015, *Nature chemistry*, 7, 301
- Pickett, H., Poynter, R., Cohen, E., et al. 1998, *Journal of Quantitative Spectroscopy and Radiative Transfer*, 60, 883
- Quan, D., & Herbst, E. 2007, *Astronomy & Astrophysics*, 474, 521
- Quénard, D., Jiménez-Serra, I., Viti, S., Holdship, J., & Coutens, A. 2018, *Monthly Notices of the Royal Astronomical Society*, 474, 2796
- Raunier, S., Chiavassa, T., Duvernay, F., et al. 2004, *Astronomy & Astrophysics*, 416, 165
- Read, W. G., Cohen, E. A., & Pickett, H. M. 1986, *Journal of Molecular Spectroscopy*, 115, 316, doi: [10.1016/0022-2852\(86\)90050-0](https://doi.org/10.1016/0022-2852(86)90050-0)
- Redondo, P., Barrientos, C., & Largo, A. 2014, *The Astrophysical Journal*, 793, 32
- Remijan, A. J., Snyder, L. E., McGuire, B. A., et al. 2014, *ApJ*, 783, 77, doi: [10.1088/0004-637X/783/2/77](https://doi.org/10.1088/0004-637X/783/2/77)
- Rimola, A., Skouteris, D., Balucani, N., et al. 2018, *ACS Earth and Space Chemistry*, 2, 720
- Rubin, R. H., Swenson, G. W., J., Benson, R. C., Tigelaar, H. L., & Flygare, W. H. 1971, *ApJL*, 169, L39, doi: [10.1086/180810](https://doi.org/10.1086/180810)
- Sakurai, M., & Yanagawa, H. 1984, *Origins of life*, 14, 171
- Saladino, R., Crestini, C., Pino, S., Costanzo, G., & Di Mauro, E. 2012, *Physics of Life Reviews*, 9, 84, doi: [10.1016/j.plrev.2011.12.002](https://doi.org/10.1016/j.plrev.2011.12.002)
- Skouteris, D., Vazart, F., Ceccarelli, C., et al. 2017, *Monthly Notices of the Royal Astronomical Society: Letters*, 468, L1
- Snyder, L. E., & Buhl, D. 1972, *ApJ*, 177, 619, doi: [10.1086/151739](https://doi.org/10.1086/151739)
- Spall, B., & Steacie, E. W. R. 1957, *Proceedings of the Royal Society of London. Series A. Mathematical and Physical Sciences*, 239, 1
- Tideswell, D., Fuller, G., Millar, T., & Markwick, A. 2010, *Astronomy & Astrophysics*, 510, A85
- Turner, B. 1991, *The Astrophysical Journal Supplement Series*, 76, 617
- Turner, B. E., Liszt, H. S., Kaifu, N., & Kisliakov, A. G. 1975, *ApJL*, 201, L149, doi: [10.1086/181963](https://doi.org/10.1086/181963)
- Vorob'eva, E., & Dyubko, S. 1994, *Radiophysics and quantum electronics*, 37, 155
- White, G. J., Araki, M., Greaves, J., Ohishi, M., & Higginbottom, N. 2003, *Astronomy & Astrophysics*, 407, 589
- Xue, C., Remijan, A. J., Brogan, C. L., et al. 2019, *ApJ*, 882, 118, doi: [10.3847/1538-4357/ab32e0](https://doi.org/10.3847/1538-4357/ab32e0)
- Zeng, S., Jiménez-Serra, I., Rivilla, V., et al. 2018, *Monthly Notices of the Royal Astronomical Society*, 478, 2962
- Zernickel, A., Schilke, P., Schmiedeke, A., et al. 2012, *A&A*, 546, A87, doi: [10.1051/0004-6361/201219803](https://doi.org/10.1051/0004-6361/201219803)

## APPENDIX

## A. CHEMICAL STRUCTURE AND NAMING OF AMIDES

According to the definition given by the International Union of Pure and Applied Chemistry (IUPAC), amides are oxoacids, which follow the general chemical formula  $-E(=O)(OH)$  ( $E$  = carbon, sulphur, or other atom that can make this bond), in which the OH group has been replaced by an  $NH_x$  group. Proper amides are therefore molecules that, for example, follow the structures  $R_1-C(=O)N-R_2R_3$ . However, several molecules that do not adhere to this structure are also called amides, such as cyanamide ( $NH_2CN$ ). Despite technically not being an amide, cyanamide and the other amides covered in this work do share a distinct chemical structure by which they can be grouped together.

All amides discussed in this work have structures involving a double ( $C=O$ ) or triple bonded ( $C\equiv N$ ) group attached to a  $-NH_2$  group. The molecular orbitals of these fragments are quite different. The double or triple bonded carbon atom and its counterpart have a flat  $SP^2$  and  $SP$  hybridized molecular orbital, respectively. Normally, a  $-NH_2$  group will have a tetrahedral  $SP^3$  orbital, similar to for example methane ( $CH_4$ ). Two molecular fragments that form a bond through a  $SP^2$  or  $SP$  hybridized orbital will form a rigid structure, but fragments that form a bond through a  $SP^3$  orbital can usually freely rotate around the bond axis. However, in the case of an amide, the  $-NH_2$  group is attached to a carbon atom with  $SP^2$  or  $SP$  orbital, causing it to take on an  $SP^2$  character, forming a so-called resonance hybrid. This effectively means that the  $(C=X)-NH_2$  bond in an amide takes on a double bond character and becomes a rigid and flat structure. This chemical structure is found in the proper amides (e.g.,  $NH_2CHO$ ), but also in cyanamide ( $NH_2CN$ ), thus making this a distinct feature of this group of molecules.

## B. SPECTROSCOPIC LINELISTS

Spectroscopic linelists used in the work are primarily taken from the CDMS database, but several list from the JPL spectroscopic database and literature sources are used as well. Table 4 gives an overview of the catalogues and identifiers for each molecule analyzed in this work and the main works these entries are based on.

**Table 4.** Linelists and spectroscopic literature

Molecule	Catalogue & ID	Literature
NH <sub>2</sub> CN	JPL 42003	Read et al. (1986)
HN <sup>12</sup> CO	CDMS 43511	Kukolich et al. (1971) Hocking et al. (1975) Niedenhoff et al. (1995) Lapinov et al. (2007)
HN <sup>13</sup> CO	JPL 44008	Hocking et al. (1975)
NH <sub>2</sub> <sup>12</sup> CHO	CDMS 45512	Motiyenko et al. (2012) Kryvda et al. (2009) Blanco et al. (2006) Vorob'eva & Dyubko (1994) Moskienko & Dyubko (1991) Gardner et al. (1980) Hirota et al. (1974) Kukolich & Nelson (1971)
NH <sub>2</sub> <sup>13</sup> CHO	CDMS 46512	Motiyenko et al. (2012) Gardner et al. (1980) Blanco et al. (2006) Kryvda et al. (2009)
CH <sub>3</sub> C(O)NH <sub>2</sub>	Literature	Ilyushin et al. (2004)
CH <sub>3</sub> NHCHO	Literature	Belloche et al. (2017)
NH <sub>2</sub> C(O)NH <sub>2</sub>	CDMS 60517	Remijan et al. (2014) Brown et al. (1975) Kasten & Dreizler (1986) Kretschmer et al. (1996)

## C. IDENTIFIED SPECTRAL LINES

**Table 5.** Overview of spectral lines of amides molecules toward NGC 6334I

Molecule	transition $J', K'_a, K'_c - J'', K''_a, K''_c$	Frequency <sup>†</sup> (MHz)	$A_{ij}$ (s <sup>-1</sup> )	$E_{up}$ (K)
NH <sub>2</sub> CN	14 4 11 - 13 4 10	279 479.5918 (0.0066)	$2.05 \times 10^{-3}$	398
	14 4 10 - 13 4 9	279 479.5921 (0.0066)	$2.05 \times 10^{-3}$	398
	14 0 14 - 13 0 13	279 600.4593 (0.0049)	$2.24 \times 10^{-3}$	172
	14 4 10 - 13 4 9	279 763.3778 (0.0056)	$2.12 \times 10^{-3}$	332
	14 4 11 - 13 4 10	279 763.3778 (0.0056)	$2.12 \times 10^{-3}$	332
	14 0 14 - 13 0 13	279 818.8464 (0.0060)	$2.30 \times 10^{-3}$	101
	14 2 13 - 13 2 12	279 820.8787 (0.0037)	$2.26 \times 10^{-3}$	159

**Table 5** *continued*

**Table 5** (*continued*)

Molecule	transition	Frequency <sup>†</sup>	$A_{ij}$	$E_{up}$
	$J', K'_a, K'_c - J'', K''_a, K''_c$	(MHz)	(s <sup>-1</sup> )	(K)
	14 2 12 - 13 2 11	279 900.1968 (0.0037)	$2.26 \times 10^{-3}$	159
	14 3 12 - 13 3 11	280 133.2385 (0.0044)	$2.23 \times 10^{-3}$	231
	14 3 11 - 13 3 10	280 137.4694 (0.0044)	$2.23 \times 10^{-3}$	231
	17 1 17 - 16 1 16	337 561.3190 (0.0059)	$4.06 \times 10^{-3}$	160
	17 2 16 - 16 2 15	339 122.8867 (0.0056)	$3.90 \times 10^{-3}$	274
	17 4 14 - 16 4 13	339 347.0172 (0.0078)	$3.80 \times 10^{-3}$	444
	17 0 17 - 16 0 16	339 450.5912 (0.0063)	$4.04 \times 10^{-3}$	218
	17 2 16 - 16 2 15	339 750.7631 (0.0046)	$4.09 \times 10^{-3}$	205
HN <sup>12</sup> CO	6 1 6 - 5 1 5	131 394.2300 (0.0004)	$2.92 \times 10^{-5}$	65
	6 4 2 - 5 4 1	131 733.5888 (0.0029)	$1.41 \times 10^{-5}$	673
	6 4 3 - 5 4 2	131 733.5888 (0.0029)	$1.41 \times 10^{-5}$	673
	6 3 4 - 5 3 3	131 799.2971 (0.0024)	$2.07 \times 10^{-5}$	397
	6 3 3 - 5 3 2	131 799.2972 (0.0024)	$2.07 \times 10^{-5}$	397
	6 2 5 - 5 2 4	131 845.8900 (0.0014)	$2.61 \times 10^{-5}$	192
	6 2 4 - 5 2 3	131 846.5998 (0.0014)	$2.61 \times 10^{-5}$	192
	6 0 6 - 5 0 6	131 885.7341 (0.0005)	$3.08 \times 10^{-5}$	22
	16 1 16 - 15 1 15	350 333.0590 (0.0100)	$5.97 \times 10^{-4}$	186
	16 3 13 - 15 3 12	351 416.8123 (0.0052)	$5.31 \times 10^{-4}$	518
	16 3 14 - 15 3 13	351 416.7983 (0.0052)	$5.31 \times 10^{-4}$	518
	16 2 15 - 15 2 14	351 537.7954 (0.0030)	$5.75 \times 10^{-4}$	314
	16 2 14 - 15 2 13	351 551.5731 (0.0032)	$5.75 \times 10^{-4}$	314
	16 0 16 - 15 0 15	351 633.2570 (0.0100)	$6.13 \times 10^{-4}$	143
	40 1 40 - 39 1 39	875 046.1710 (0.0031)	$9.50 \times 10^{-3}$	905
	40 3 38 - 39 3 37	877 808.5933 (0.0111)	$8.68 \times 10^{-3}$	1239
	40 3 37 - 39 3 36	877 809.9771 (0.0112)	$8.68 \times 10^{-3}$	1239
	40 2 39 - 39 2 38	878 062.2368 (0.0063)	$9.25 \times 10^{-3}$	1035
	40 0 40 - 39 0 39	878 137.4392 (0.0029)	$9.72 \times 10^{-3}$	864
	40 2 38 - 39 2 37	878 276.9143 (0.0065)	$9.26 \times 10^{-3}$	1035
	41 1 41 - 40 1 40	896 873.8160 (0.0150)	$1.02 \times 10^{-2}$	948
HN <sup>13</sup> CO	6 1 6 - 5 1 5	131 397.0955 (0.0084)	$2.96 \times 10^{-5}$	65
	6 0 6 - 5 0 5	131 889.4868 (0.0128)	$3.06 \times 10^{-5}$	22
	16 1 16 - 15 1 15	350 340.3407 (0.0908)	$6.18 \times 10^{-4}$	186
	16 0 16 - 15 0 15	351 642.8746 (0.0763)	$6.27 \times 10^{-4}$	143
NH <sub>2</sub> <sup>12</sup> CHO	6 1 5 - 5 1 4	131 617.9025 (0.0005)	$1.56 \times 10^{-4}$	25
	25 2 23 - 25 1 24	280 689.4724 (0.0009)	$5.21 \times 10^{-5}$	351
	12 5 8 - 13 4 9	281 381.6715 (0.0012)	$1.04 \times 10^{-5}$	154
	15 2 14 - 15 1 15	281 934.6250 (0.0008)	$3.40 \times 10^{-5}$	134
	14 3 11 - 14 2 12	282 822.5932 (0.0009)	$5.44 \times 10^{-5}$	134
	15 2 14 - 15 0 15	294 753.3491 (0.0008)	$1.07 \times 10^{-5}$	134
	14 2 13 - 13 2 12	294 776.9896 (0.0009)	$1.84 \times 10^{-3}$	118

**Table 5** *continued*



**Table 5** (*continued*)

Molecule	transition	Frequency <sup>†</sup>	$A_{ij}$	$E_{up}$
	$J', K'_a, K'_c - J'', K''_a, K''_c$	(MHz)	(s <sup>-1</sup> )	(K)
	17 3 15 - 17 2 16	336 733.0134 (0.0009)	$8.20 \times 10^{-5}$	183
	16 13 3 - 15 13 2	339 746.2586 (0.0023)	$9.84 \times 10^{-4}$	640
	16 13 4 - 15 13 3	339 746.2586 (0.0023)	$9.84 \times 10^{-4}$	640
	16 7 10 - 15 7 9	339 779.5370 (0.0300)	$2.34 \times 10^{-3}$	284
	16 7 9 - 15 7 8	339 779.5370 (0.0300)	$2.34 \times 10^{-3}$	284
	16 2 14 - 15 2 13	349 478.2047 (0.0009)	$3.10 \times 10^{-3}$	153
	9 2 8 - 8 1 7	349 634.0304 (0.0012)	$6.22 \times 10^{-5}$	58
	41 7 34 - 40 7 33	874 836.2150 (0.0500)	$4.89 \times 10^{-2}$	1025
	42 2 40 - 41 2 39	875 818.8790 (0.0500)	$5.01 \times 10^{-2}$	940
	15 5 10 - 14 4 11	876 148.3790 (0.0500)	$1.11 \times 10^{-3}$	197
	41 5 37 - 40 5 36	876 252.7700 (0.0500)	$4.98 \times 10^{-2}$	956
	41 6 36 - 40 6 35	876 493.3340 (0.0500)	$4.95 \times 10^{-2}$	988
	41 6 35 - 40 6 34	878 706.9000 (0.0500)	$4.99 \times 10^{-2}$	988
	22 3 19 - 21 2 20	879 169.0967 (0.0022)	$3.84 \times 10^{-4}$	287
	42 13 29 - 41 13 28	891 600.4990 (0.0500)	$4.82 \times 10^{-2}$	1422
	42 13 30 - 41 13 29	891 600.4990 (0.0500)	$4.82 \times 10^{-2}$	1422
	43 3 41 - 42 3 40	893 045.4010 (0.0500)	$5.32 \times 10^{-2}$	983
	45 0 45 - 44 1 44	893 077.5610 (0.0500)	$2.76 \times 10^{-3}$	997
	45 1 45 - 44 1 44	893 083.8870 (0.0500)	$5.35 \times 10^{-2}$	997
	45 0 45 - 44 0 44	893 085.9940 (0.0500)	$5.35 \times 10^{-2}$	997
	45 1 45 - 44 0 44	893 092.3230 (0.0500)	$2.76 \times 10^{-3}$	997
	44 2 43 - 43 2 42	893 184.3320 (0.0500)	$5.34 \times 10^{-2}$	992
	42 9 34 - 41 9 33	893 415.4200 (0.0500)	$5.12 \times 10^{-2}$	1162
	42 9 33 - 41 9 32	893 415.4200 (0.0500)	$5.12 \times 10^{-2}$	1162
	42 8 35 - 41 8 34	894 533.0350 (0.0500)	$5.19 \times 10^{-2}$	1112
	42 8 34 - 41 8 33	894 550.9190 (0.0500)	$5.19 \times 10^{-2}$	1112
	43 2 41 - 42 2 40	895 080.2490 (0.0500)	$5.35 \times 10^{-2}$	983
NH <sub>2</sub> <sup>13</sup> CHO	6 1 5 - 5 1 4	131 495.8540 (0.0100)	$1.55 \times 10^{-4}$	25
	13 1 12 - 12 1 11	282 107.1134 (0.0026)	$1.63 \times 10^{-3}$	98
	14 1 14 - 13 1 13	282 693.5048 (0.0027)	$1.65 \times 10^{-3}$	105
	16 8 8 - 15 8 7	339 213.4944 (0.0029)	$2.16 \times 10^{-3}$	324
	16 8 9 - 15 8 8	339 213.4944 (0.0029)	$2.16 \times 10^{-3}$	324
	16 2 14 - 15 2 13	349 308.8534 (0.0030)	$3.10 \times 10^{-3}$	153
CH <sub>3</sub> C(O)NH <sub>2</sub>	23 10 14 - 22 9 13	351 083.4533 (0.0458)	$2.12 \times 10^{-3}$	235
	22 10 12 - 21 11 11	351 097.8247 (0.0412)	$1.89 \times 10^{-3}$	225
	22 11 12 - 21 10 11	351 097.8510 (0.0412)	$1.89 \times 10^{-3}$	225
	24 8 16 - 23 9 15	351 134.2229 (0.0499)	$2.32 \times 10^{-3}$	244
	24 9 16 - 23 8 15	351 134.2229 (0.0499)	$2.32 \times 10^{-3}$	244
	25 7 18 - 24 8 17	351 214.4618 (0.0534)	$2.51 \times 10^{-3}$	253
	25 8 18 - 24 7 17	351 214.4618 (0.0534)	$2.51 \times 10^{-3}$	253

**Table 5** *continued*

**Table 5** (*continued*)

Molecule	transition	Frequency <sup>†</sup>	$A_{ij}$	$E_{up}$
	$J', K'_a, K'_c - J'', K''_a, K''_c$	(MHz)	(s <sup>-1</sup> )	(K)
	26 6 20 - 25 7 19	351 309.0658 (0.0563)	$2.69 \times 10^{-3}$	260
	26 7 20 - 25 6 19	351 309.0658 (0.0563)	$2.69 \times 10^{-3}$	260
	29 3 26 - 28 4 25	351 621.6370 (0.0657)	$3.18 \times 10^{-3}$	276
	29 4 26 - 28 3 25	351 621.6370 (0.0657)	$3.18 \times 10^{-3}$	276
	31 1 30 - 30 2 29	351 830.6986 (0.0819)	$3.47 \times 10^{-3}$	282
	31 2 30 - 30 1 29	351 830.6986 (0.0819)	$3.47 \times 10^{-3}$	282
CH <sub>3</sub> NHCHO	11 3 8 - 10 3 7 <sup>‡</sup>	130 190.7247 (0.0009)	$9.21 \times 10^{-5}$	43
	12 2 11 - 11 2 10	130 874.1508 (0.0010)	$9.75 \times 10^{-5}$	44
	11 2 9 - 10 2 8 <sup>‡</sup>	131 427.7286 (0.0009)	$9.86 \times 10^{-5}$	40
	13 8 5 - 12 8 4	144 416.877 (0.0014)	$8.97 \times 10^{-5}$	97
	9 7 2 - 8 6 2	279 381.6637 (0.0035)	$5.18 \times 10^{-4}$	62
	25 12 13 - 24 12 12 <sup>‡</sup>	280 384.9819 (0.0041)	$8.20 \times 10^{-4}$	274
	25 14 11 - 24 14 11 <sup>‡</sup>	280 716.5012 (0.0202)	$6.82 \times 10^{-4}$	308
	25 10 15 - 24 10 14	280 743.3675 (0.0049)	$8.94 \times 10^{-4}$	245
	24 5 19 - 23 5 18 <sup>‡</sup>	280 994.8045 (0.0021)	$9.96 \times 10^{-4}$	186
	25 13 13 - 24 13 12	281 110.7375 (0.0045)	$7.76 \times 10^{-4}$	291
	25 13 12 - 24 13 11	281 113.0259 (0.0046)	$7.81 \times 10^{-4}$	291
	25 11 14 - 24 11 13	282 584.3703 (0.0088)	$8.55 \times 10^{-4}$	259
	26 9 17 - 25 9 16	291 978.5554 (0.0027)	$1.06 \times 10^{-3}$	247
	26 12 14 - 25 12 13	292 546.3434 (0.0055)	$9.46 \times 10^{-4}$	288
	26 5 22 - 25 5 21	292 648.065 (0.0023)	$1.13 \times 10^{-3}$	211
	26 15 11 - 25 15 10 <sup>‡</sup>	292 847.7083 (0.0108)	$8.05 \times 10^{-4}$	341
	25 5 20 - 24 5 19	293 006.2032 (0.0023)	$1.14 \times 10^{-3}$	200
	8 8 0 - 7 7 0	294 241.2632 (0.0049)	$7.64 \times 10^{-4}$	67
	34 0 34 - 33 0 33	337 907.4314 (0.0048)	$1.30 \times 10^{-3}$	291
	34 1 34 - 33 1 33	337 907.4314 (0.0048)	$1.30 \times 10^{-3}$	291
	34 1 34 - 33 0 33	337 907.4314 (0.0048)	$1.30 \times 10^{-3}$	291
	34 0 34 - 33 1 33	337 907.4314 (0.0048)	$1.30 \times 10^{-3}$	291
	30 10 20 - 29 10 19 <sup>‡</sup>	337 993.2492 (0.0041)	$1.61 \times 10^{-3}$	321
	30 4 26 - 29 4 25	338 606.6396 (0.0028)	$1.74 \times 10^{-3}$	272
	29 6 23 - 28 6 22	348 416.9795 (0.0029)	$1.89 \times 10^{-3}$	268
	31 4 27 - 30 4 26	348 417.6722 (0.009)	$1.39 \times 10^{-3}$	288
	30 5 25 - 29 5 24	348 837.7283 (0.0030)	$1.94 \times 10^{-3}$	279
	31 5 27 - 30 4 26 <sup>‡</sup>	350 710.9037 (0.0031)	$7.43 \times 10^{-4}$	288
NH <sub>2</sub> C(O)NH <sub>2</sub>	25 3 23 - 24 2 22	279 472.8671 (0.0468)	$2.55 \times 10^{-4}$	195
	25 2 23 - 24 2 22	279 472.8671 (0.0468)	$1.25 \times 10^{-3}$	195
	25 3 23 - 24 3 22	279 472.8671 (0.0468)	$1.25 \times 10^{-3}$	195
	25 2 23 - 24 3 22	279 472.8671 (0.0468)	$2.55 \times 10^{-4}$	195
	24 5 20 - 23 4 19	282 190.8684 (0.0399)	$1.20 \times 10^{-3}$	199
	24 5 20 - 23 5 19	282 190.8684 (0.0399)	$2.16 \times 10^{-4}$	199

**Table 5** *continued*

**Table 5** (*continued*)

Molecule	transition	Frequency <sup>†</sup>	$A_{ij}$	$E_{up}$
	$J', K'_a, K'_c - J'', K''_a, K''_c$	(MHz)	(s <sup>-1</sup> )	(K)
	24 4 20 - 23 4 19	282 190.8684 (0.0399)	$2.16 \times 10^{-4}$	199
	24 4 20 - 23 5 19	282 190.8684 (0.0399)	$1.20 \times 10^{-3}$	199
	25 4 21 - 24 4 20	290 862.3844 (0.0473)	$1.48 \times 10^{-3}$	213
	25 4 21 - 24 5 20	290 862.3844 (0.0473)	$9.83 \times 10^{-5}$	213
	25 5 21 - 24 5 20	290 862.3844 (0.0473)	$9.83 \times 10^{-5}$	213
	25 5 21 - 24 4 20	290 862.3844 (0.0473)	$1.48 \times 10^{-3}$	213
	22 7 16 - 21 6 15	293 236.5715 (0.0337)	$1.18 \times 10^{-3}$	186
	22 6 16 - 21 7 15	293 236.5646 (0.0337)	$1.18 \times 10^{-3}$	186
	21 7 14 - 20 8 13	293 292.5803 (0.0297)	$1.05 \times 10^{-3}$	179
	21 8 14 - 20 7 13	293 293.5513 (0.0297)	$1.05 \times 10^{-3}$	179
	24 5 19 - 23 5 18	293 642.0215 (0.0385)	$1.01 \times 10^{-4}$	208
	24 6 19 - 23 5 18	293 642.0215 (0.0385)	$1.39 \times 10^{-3}$	208
	24 5 19 - 23 6 18	293 642.0215 (0.0385)	$1.39 \times 10^{-3}$	208
	24 6 19 - 23 6 18	293 642.0215 (0.0385)	$1.01 \times 10^{-4}$	208

NOTE—<sup>†</sup>The uncertainty of each line frequency is given in the parentheses. <sup>‡</sup>CH<sub>3</sub>NHCHO lines that are present on locations where the baseline dips.

#### D. SPECTRAL FEATURES TOWARD MM1-I AND MM2-I

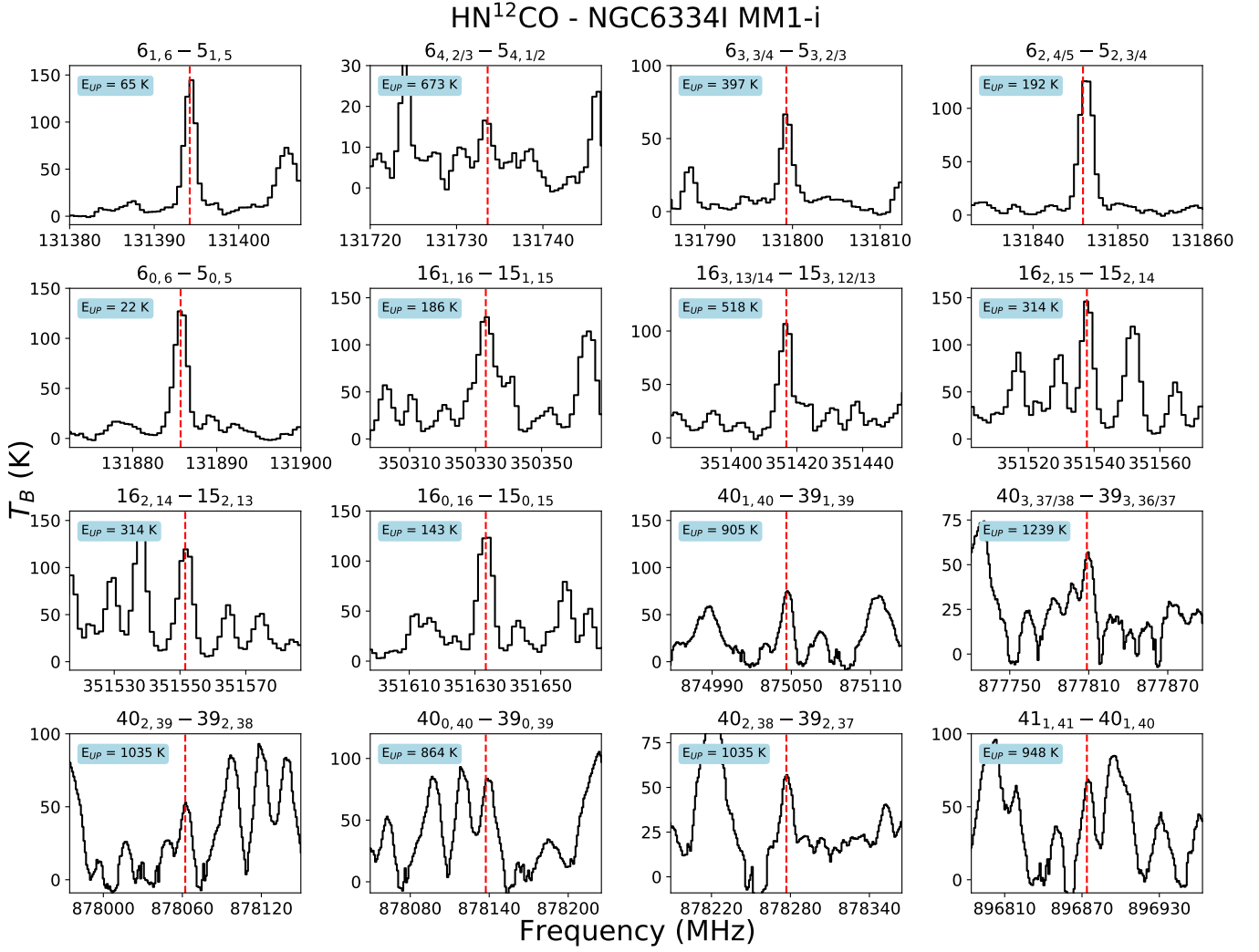


**Figure 9.** Detected transitions of HN<sup>12</sup>CO in the spectrum toward position MM1-i. The observed spectrum is plotted in black and the rest frequency center of the transition is indicated by the red dotted line. Because these lines are optically thick, they are not fitted with a synthetic spectrum. The upper state energy of each transition is given in the top left corner.

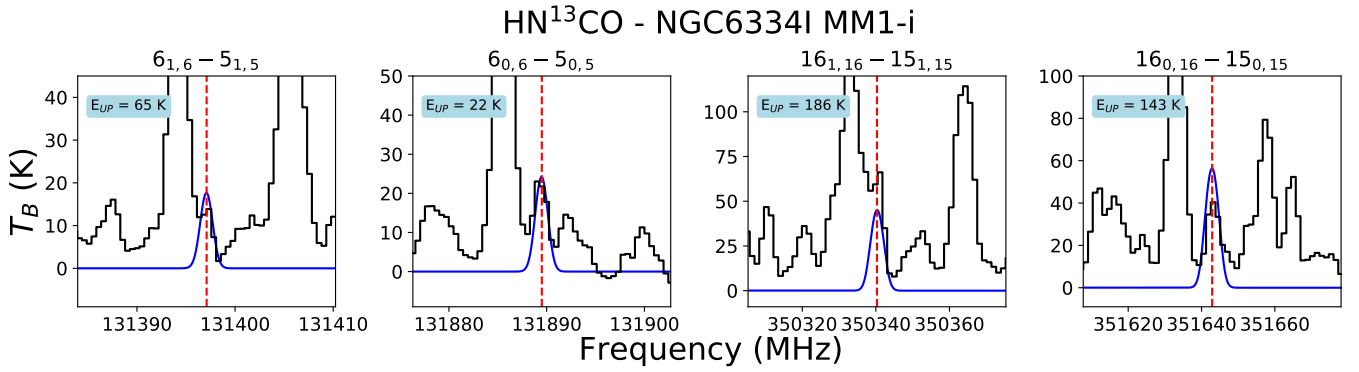


**Figure 10.** Detected transitions of HN<sup>13</sup>CO in the spectrum toward position MM1-i. The observed spectrum is plotted in black, with the synthetic spectrum overplotted in blue and the rest frequency center of the transition is indicated by the red dotted line. The upper state energy of each transition is given in the top left corner.

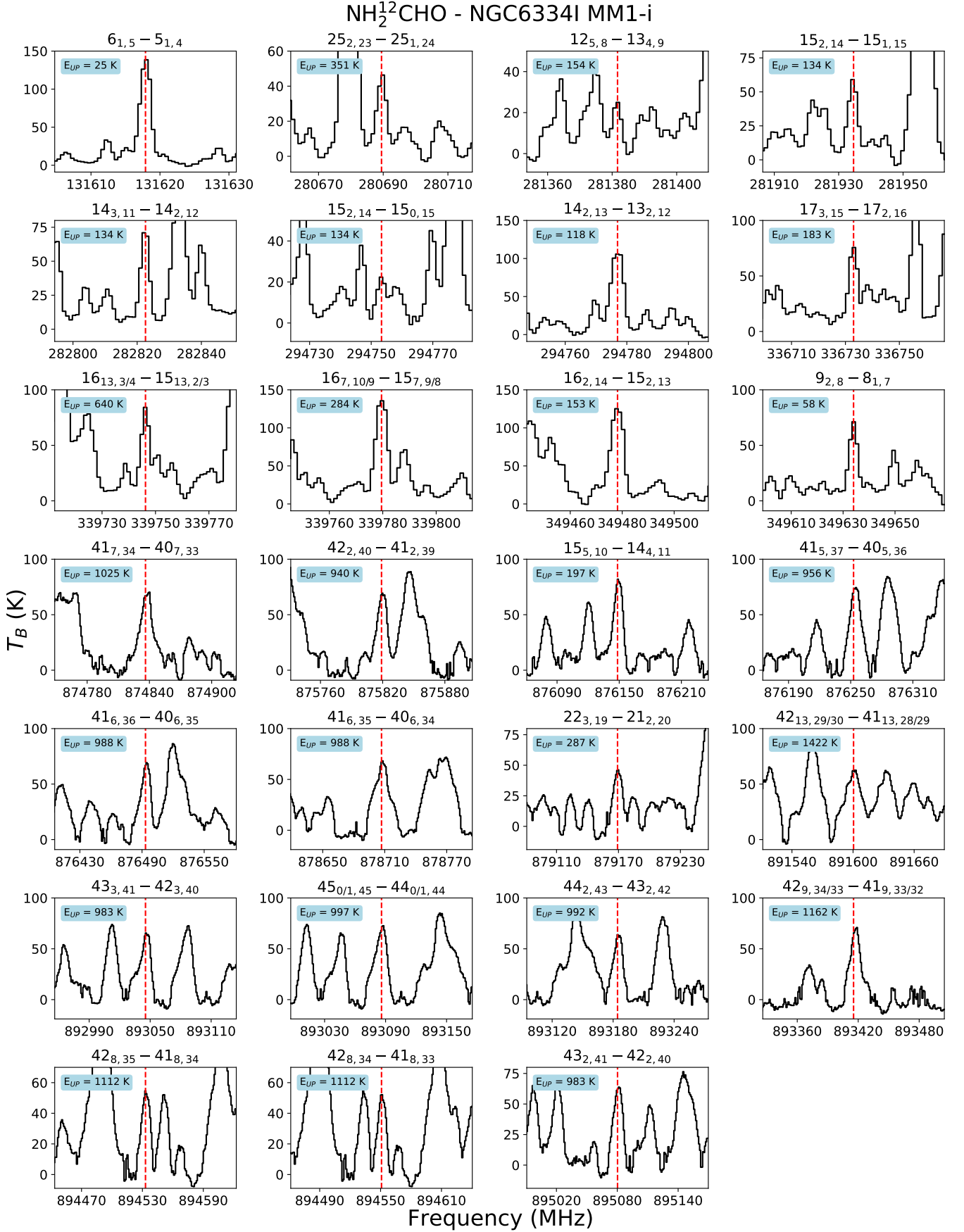


**Figure 11.** Detected transitions of  $\text{NH}_2^{12}\text{CHO}$  in the spectrum toward position MM1-i. The observed spectrum is plotted in black and the rest frequency center of the transition is indicated by the red dotted line. Because these lines are optically thick, they are not fitted with a synthetic spectrum. The upper state energy of each transition is given in the top left corner.



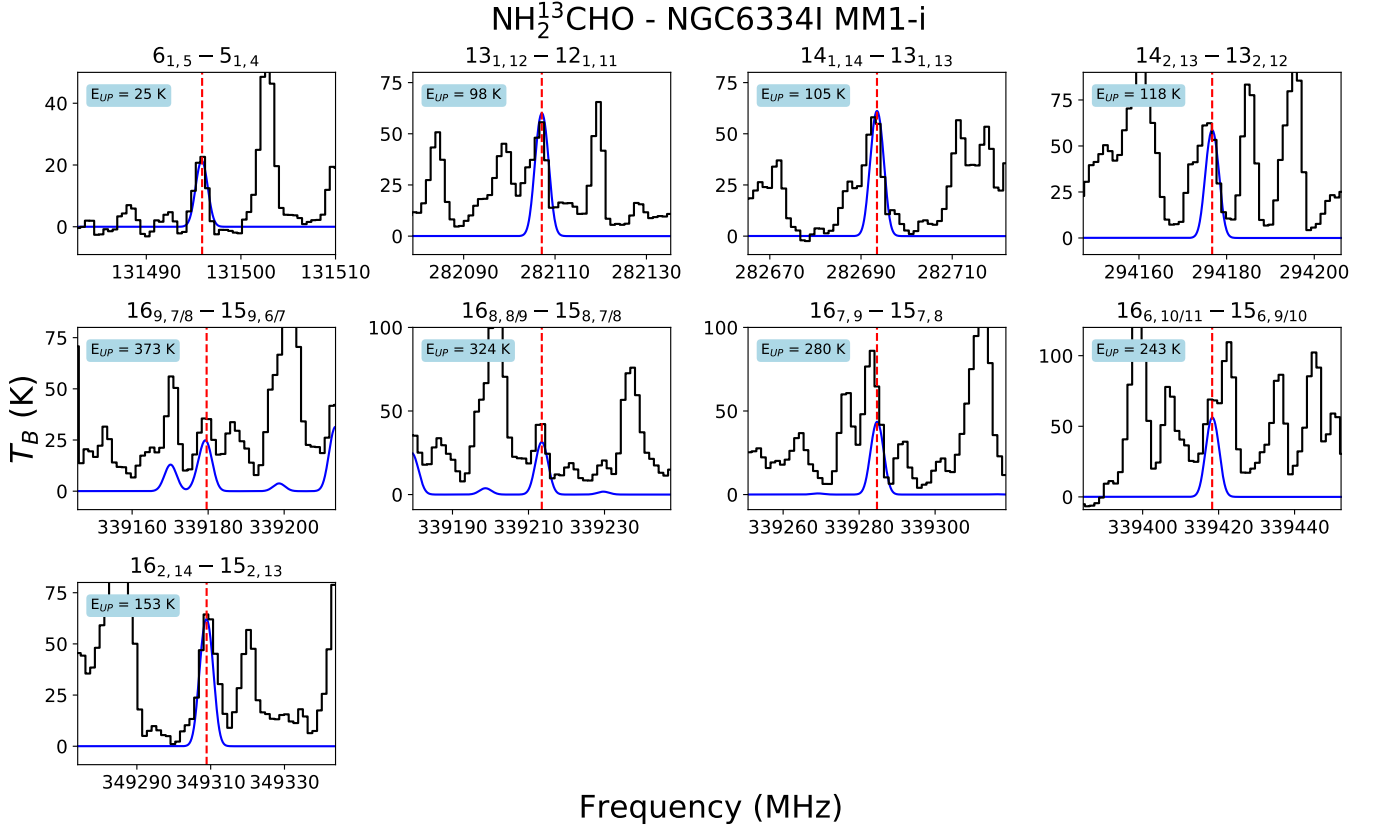


**Figure 12.** Detected transitions of NH<sub>2</sub><sup>13</sup>CHO in the spectrum toward position MM1-i. The observed spectrum is plotted in black, with the synthetic spectrum overlotted in blue and the rest frequency center of the transition is indicated by the red dotted line. The upper state energy of each transition is given in the top left corner.

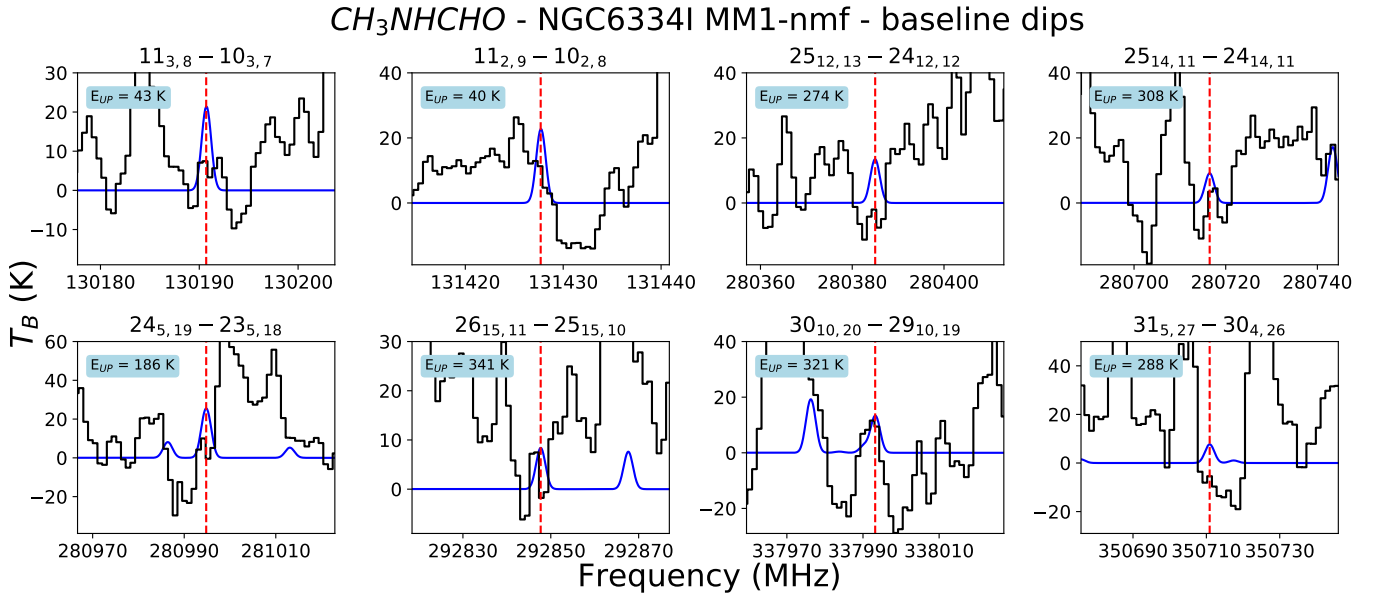


**Figure 13.** Transitions of CH<sub>3</sub>NHCHO that are missing in the spectrum toward position MM1-nmf due to baseline dips. The observed spectrum is plotted in black, with the synthetic spectrum overlotted in blue and the rest frequency center of the transition is indicated by the red dotted line. The upper state energy of each transition is given in the top left corner.

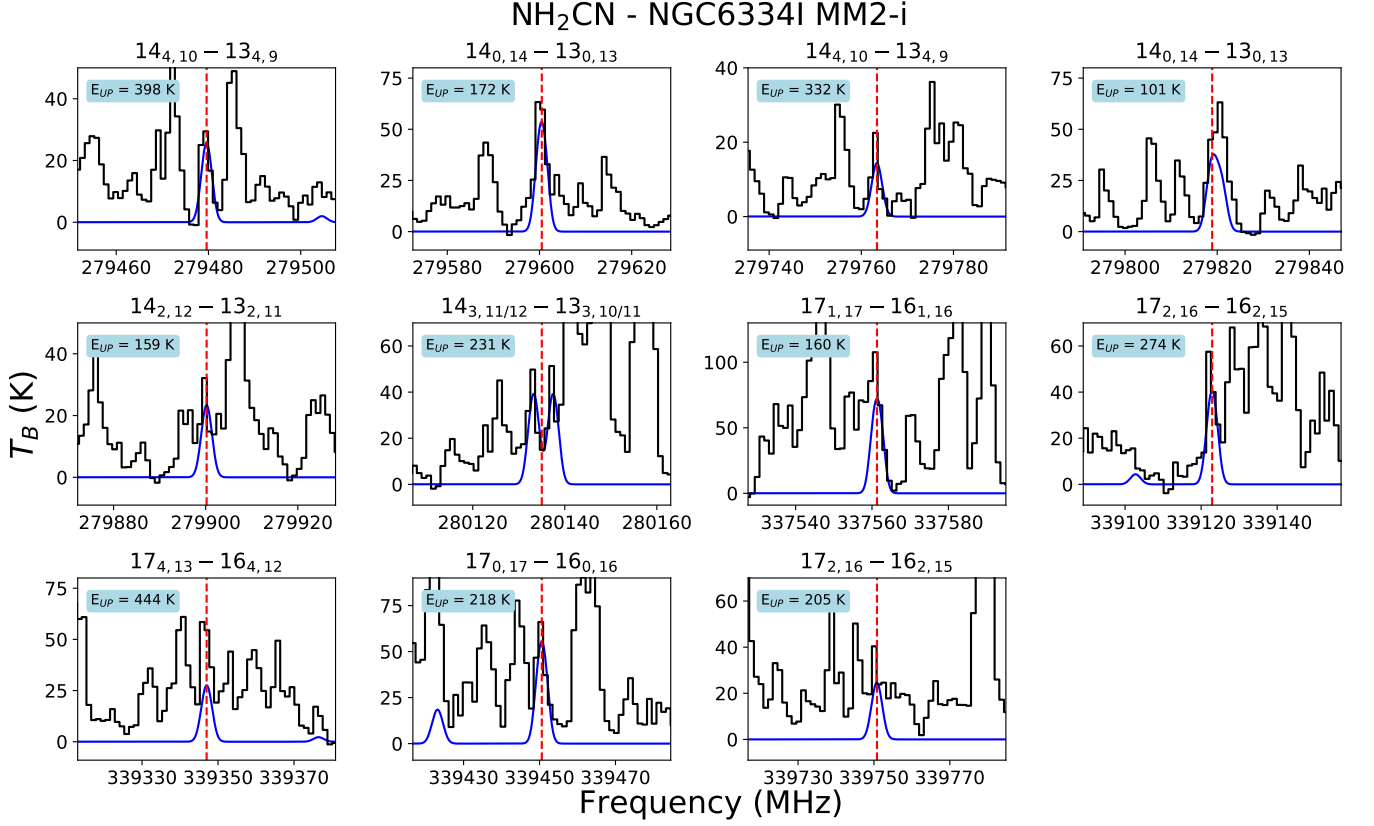


**Figure 14.** Detected transitions of NH<sub>2</sub>CN in the spectrum toward position MM2-i. The observed spectrum is plotted in black, with the synthetic spectrum overplotted in blue and the rest frequency center of the transition is indicated by the red dotted line. The upper state energy of each transition is given in the top left corner.

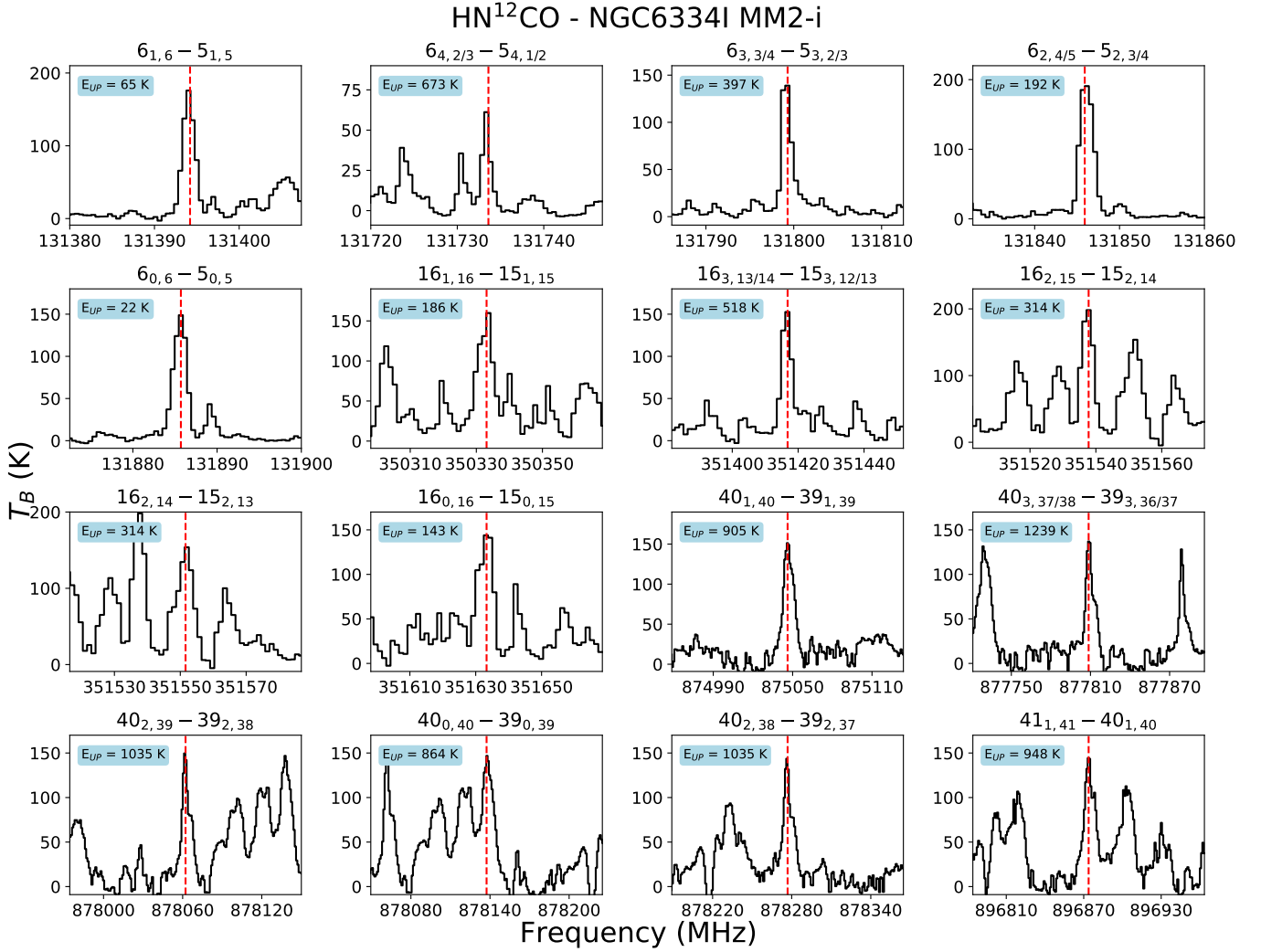


**Figure 15.** Detected transitions of HN<sup>12</sup>CO in the spectrum toward position MM2-i. The observed spectrum is plotted in black and the rest frequency center of the transition is indicated by the red dotted line. Because these lines are optically thick, they are not fitted with a synthetic spectrum. The upper state energy of each transition is given in the top left corner.

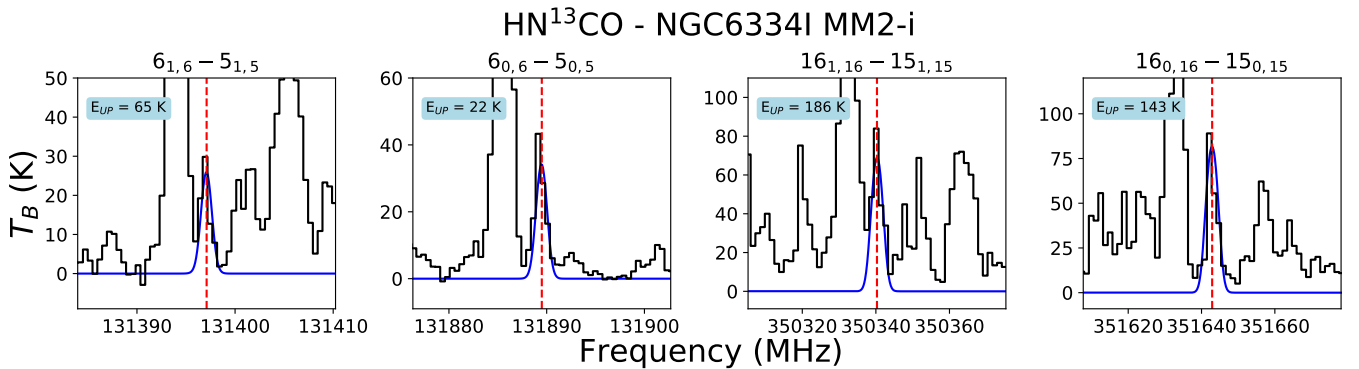


**Figure 16.** Detected transitions of HN<sup>13</sup>CO in the spectrum toward position MM2-i. The observed spectrum is plotted in black, with the synthetic spectrum overplotted in blue and the rest frequency center of the transition is indicated by the red dotted line. The upper state energy of each transition is given in the top left corner.

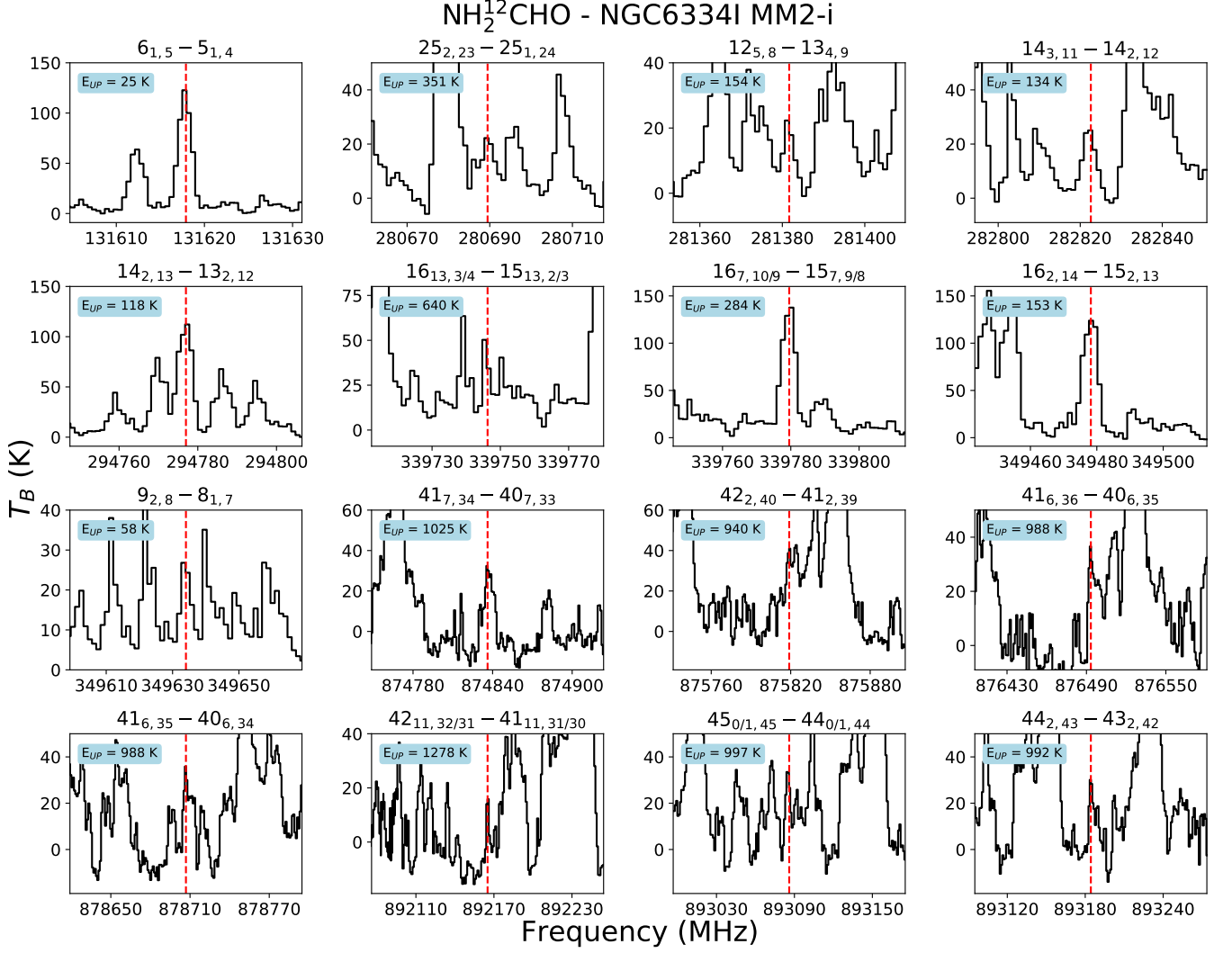


**Figure 17.** Detected transitions of  $\text{NH}_2^{12}\text{CHO}$  in the spectrum toward position MM2-i. The observed spectrum is plotted in black the rest frequency center of the transition is indicated by the red dotted line. Because these lines are optically thick, they are not fitted with a synthetic spectrum. The upper state energy of each transition is given in the top left corner.

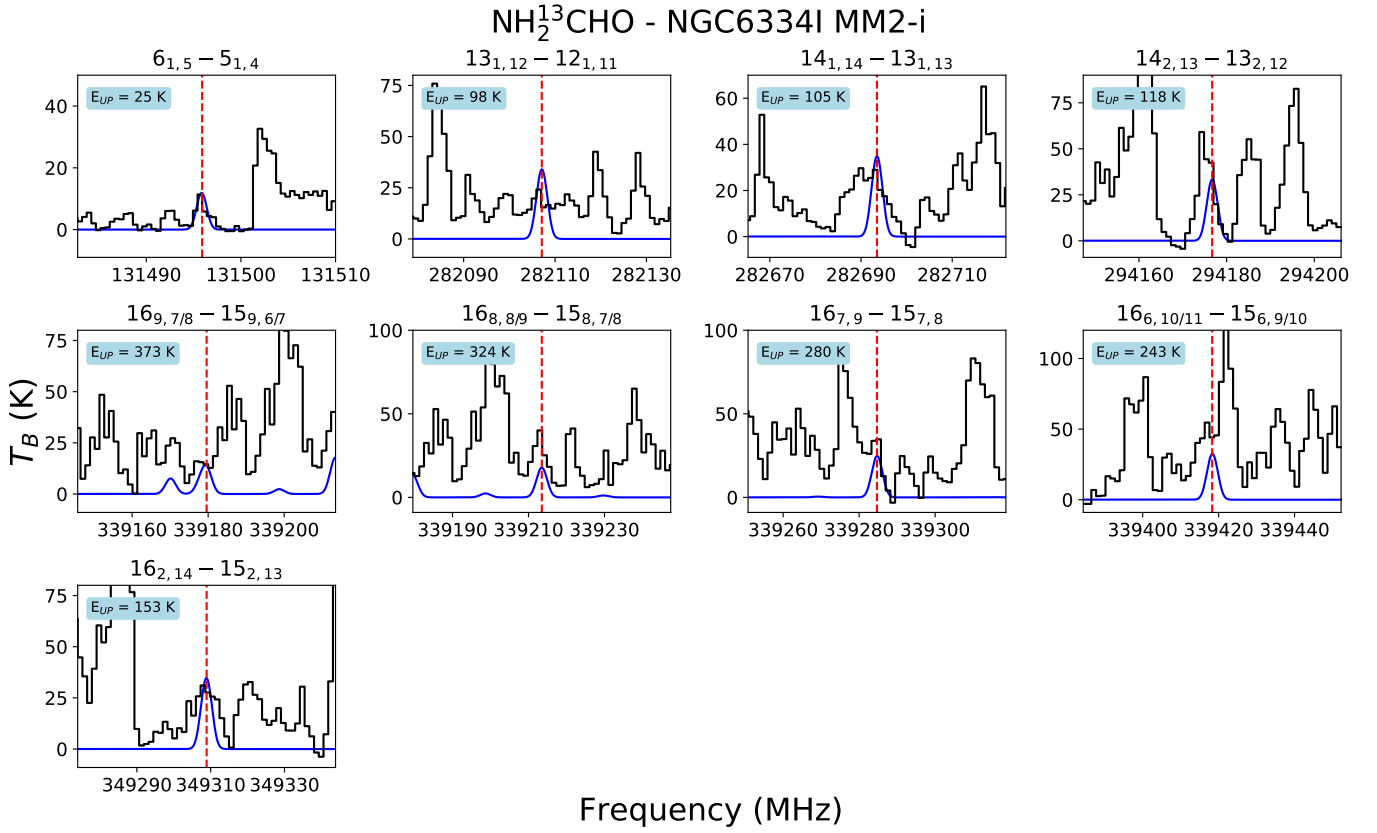


**Figure 18.** Detected transitions of  $\text{NH}_2^{13}\text{CHO}$  in the spectrum toward position MM2-i. The observed spectrum is plotted in black, with the synthetic spectrum overplotted in blue and the rest frequency center of the transition is indicated by the red dotted line. The upper state energy of each transition is given in the top left corner.



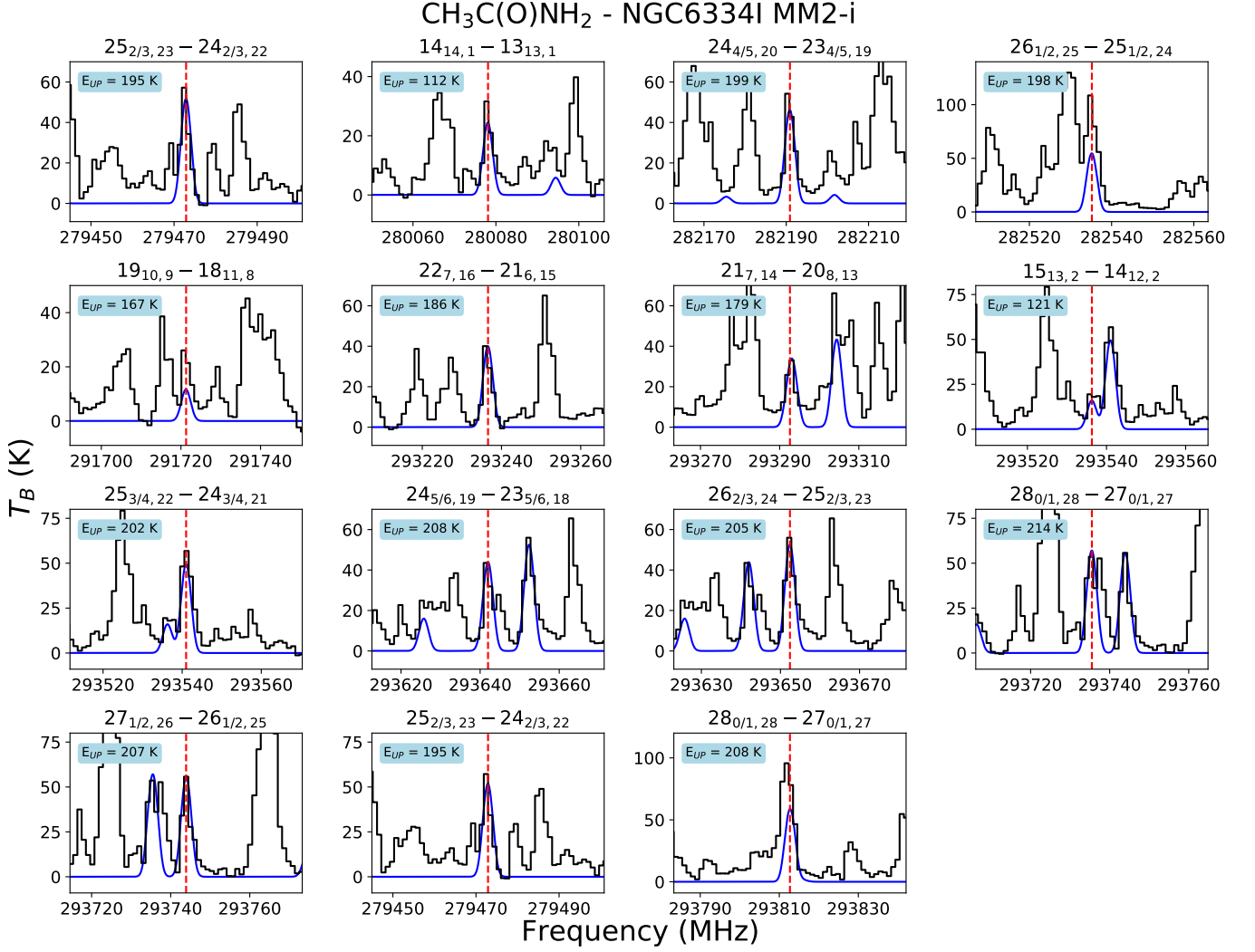


**Figure 19.** Detected transitions of CH<sub>3</sub>C(O)NH<sub>2</sub> in the spectrum toward position MM2-i. The observed spectrum is plotted in black, with the synthetic spectrum overplotted in blue and the rest frequency center of the transition is indicated by the red dotted line. The upper state energy of each transition is given in the top left corner.